nature communications

Article

https://doi.org/10.1038/s41467-024-54174-5

Mechanics-activated fibroblasts promote pulmonary group 2 innate lymphoid cell plasticity propelling silicosis progression

Received: 17 October 2023

Accepted: 5 November 2024

Yangyang He[1,2,4,5], Fan Yang[1,2,5], Lin Yang[1,2], Haoyang Yuan[1,2], Yichuan You[1,2], Yinghui Chen[1,2], Xiulin Wu[1,2], Hui Min[3], Jie Chen[1,2] ✉ & Chao Li[1,2] ✉

Crystalline silica (CS) particle exposure leads to silicosis which is characterized as progressive fibrosis. Fibroblasts are vital effector cells in fibrogenesis. Emerging studies have identified immune sentinel roles for fibroblasts in chronic disease, while their immune-modulatory roles in silicosis remain unclear. Herein, we show that group 2 innate lymphoid cell (ILC2) conversion to ILC1s is closely involved in silicosis progression, which is mediated by activated fibroblasts via interleukin (IL)−18. Mechanistically, Notch3 signaling in mechanics-activated fibroblasts modulates IL-18 production via caspase 1 activity. The mouse-specific *Notch3* knockout in fibroblasts retards pulmonary fibrosis progression that is linked to attenuated ILC conversion. Our results indicate that activated fibroblasts in silicotic lungs are regulators of ILC2−ILC1 conversion, associated with silicosis progression via the Notch3−IL-18 signaling axis. This finding broadens our understanding of immune-modulatory mechanisms in silicosis, and indicates potential therapeutic targets for lung fibrotic diseases.

Silicosis is an ancient and potentially fatal pneumoconiosis caused by respirable crystalline silica (CS) particle exposure. The disease is historically related to mining and often found amongst miners; however, a failure to recognize and control the risks associated with silica exposure in contemporary work practices, such as sandblasting denim jeans and manufacturing artificial stone benchtops, has led to the re-emergence of silicosis on a global level[1,2]. In the United States, over 1.7 million workers are exposed to CS in general, maritime, and construction industries. It is estimated that 3–5 million workers in Europe and Australia have been exposed to silica[3]; however, exposure is considerably more common in low- and middle-income countries[4]. Though CS particle exposure triggers silicosis, the mechanisms underlying disease pathology remain poorly understood. While the burden for CS-associated disease remains high, treatment options are limited.

Fibrogenesis is a hallmark of silicosis, where fibroblast activation and proliferation have dominant roles. While fibroblasts are classically immune neutral cells, whose functions are mainly related to tissue construction and extracellular matrix (ECM) remodeling, it is now clear that fibroblasts have multifaceted roles in health and disease, particularly in chronic inflammation settings[5]. Fibroblasts are now regarded as key immune sentinel cells in modulating immune responses in inflammatory diseases. Specifically, fibroblasts themselves take on different roles as inflammatory cells, recruiting leukocytes, and enabling chronic inflammation in tissues[6]. We previously reported that fibroblasts mediated interstitial macrophage polarization and recruitment[7], highlighting

---

[1]Key Laboratory of Environmental Stress and Chronic Disease Control & Prevention (China Medical University), Ministry of Education, Shenyang, Liaoning, PR China. [2]Department of Occupational and Environmental Health, School of Public Health, China Medical University, Shenyang, Liaoning, PR China. [3]Department of Immunology, College of Basic Medical Sciences, China Medical University, Shenyang, Liaoning, PR China. [4]Present address: Department of Microbiology, Immunology and Molecular Genetics, University of Texas Health Science Center San Antonio, San Antonio, TX, USA. [5]These authors contributed equally: Yangyang He, Fan Yang. ✉e-mail: jchen@cmu.edu.cn; lichao@cmu.edu.cn

an immunomodulatory role in silicosis. As major proliferating stromal cells in silicosis, the critical immunomodulatory role of fibroblasts has been underestimated.

Pulmonary immunity has an active role in silicosis pathophysiology. Myeloid cells, specifically macrophages, lymphocytes, especially T cells, in silicosis, have been widely examined[8,9], but the role of innate lymphoid cells (ILCs) remains largely unexplored. ILCs are a heterogeneous family of innate lymphocytes that, unlike T or B lymphocytes, lack antigen-specific receptor surface expression, are predominantly tissue-resident at the mucosal barrier, and can dramatically impact local tissue immunity, inflammation, and tolerance[10]. Lung ILCs are lymphocyte populations of non-T cells and non-natural killer (NK) cells that lack lineage marker (Lin^-) expression but express high CD90 (Thy-1) levels. In local tissue, ILCs not only establish first-line defenses against infection, but also orchestrate homeostatic functions via interactions with other tissue-resident cells, such as epithelial and stromal cells, or neurons[10]. Although ILCs are important for immunological protection in many infectious disease models, paradoxically, they also drive immunopathology, including that recently reported in fibrogenesis[11].

Three distinct ILC populations have been described and manifest different cytokine production and function patterns mirroring those of CD4 T helper (Th) cells[12]. Group 2 ILCs (ILC2s) are dominant in pulmonary ILC pools and produce type II cytokines (interleukin (IL)−4, IL-5, and IL-13), while group 1 ILCs (ILC1s) are characterized by interferon (IFN)-γ production, and depend on transcription factor T-bet and T-bet-dependent non-cytotoxic effects. The main cytokine produced by group 3 ILCs (ILC3s) is IL-17, which depends on the transcription factor retinoic acid receptor-related orphan receptor-γt (ROR-γt). However, ILC subsets are not stable; they can adapt to local microenvironments by changing these profiles, eliciting ILC plasticity[13], which allows them to adapt to changing local tissue conditions and tune their responses to different pathogenic stimuli. In some circumstances, ILC conversion mediates disease pathology, e.g., rheumatoid arthritis (RA) stimulation in the presence of IL-1β and IL-23 was reported to drive ILC1 plasticity and conversion to ILC3s[14], but also, in other contexts, some ILC3s converted to ILC1s[15]. In addition, ILC2s can produce IL-17 and express RORγt, which drives IL-17 expression[16]. Due to ILC plasticity, ILC1 can convert from either ex-ILC2s or ex-ILC3s, which downregulate Gata3 or RORγt, respectively, and upregulate T-bet and IFN-γ. In chronic obstruction pulmonary disease (COPD), an increased ILC1 cell frequency is correlated with disease progression, which was confirmed by direct conversion from lung resident ILC2s[17]. In silicosis, it is unclear if ILCs respond to cues in the fibrotic milieu to alter phenotypes and reshape their functions.

Here, we examine fibroblast activation with immune cell polarization, demonstrating that activated fibroblasts regulate ILC polarization and conversion in silicosis. Mechanistically, the Notch3–IL-18 axis in activated fibroblasts modulate ILC conversion. A mouse specific *Notch3* knockout (KO) in fibroblasts retards pulmonary fibrosis progression that is linked to attenuated ILC conversion. These results advance our understanding of fibroblast immunomodulatory roles, and define a pathway controlling ILC conversion in fibrotic lungs. Therefore, targeting fibroblast immune-modulatory Notch3 signaling can help limit fibrogenesis progression.

Results

CS particles in lungs activate ILCs and alter their phenotypes

To identify phenotypic changes in ILCs during silicosis pathogenesis, we established a silicosis mouse model using intratracheally-administered CS to the lungs (Fig. 1a). Flow cytometry was used to characterize immune cells isolated from mouse lung tissues. ILCs were identified as $CD45^+CD3^-Lineage^-Thy1^+$alive cells in lungs (Fig. 1b). Lineage was determined by an antibody cocktail containing CD5, CD45R (B220), CD11b, Ly-6B.2, Gr-1, and Ter-119. A surface marker expression pattern was consistent with ILCs[18,19].

We observed increased ILC percentages and cell numbers in silicotic lungs (Fig. 1c, d), implying a connection to fibrogenesis. Cytokines in the immune microenvironment also affected ILC functions; as we examined cytokine receptor expression on ILCs. ILCs in silicotic lungs expressed analogic CD127 (IL-7R) levels but decreased CD25 (IL-2Rα) and ST-2 (IL-33R) levels when compared with saline-treated lungs (Fig. 1e), implying decreased ILC responsiveness to IL-2 and IL-33 cytokines. Notably, substantially increased IL-18Rα levels in ILCs from fibrotic lungs were observed (Fig. 1f), suggesting increased ILC sensitivity to IL-18. However, IL-17RB (IL-25 receptor) was not induced on ILCs from silicotic lungs (Supplementary Fig. 1a). We also identified increased CD69, CD103, and elevated CXCR6 expression in ILCs (Fig. 1g), manifesting as enhanced immobilization in fibrotic lungs. The chemokine receptor CCR9, expressed by ILC precursors, was unaffected and indicated that ILCs were not recruited from the circulation (Supplementary Fig. 1b).

To gain more insights, we also examined effector molecule expression on ILCs. Notably, ILCs from fibrotic lungs expressed elevated MHC-II levels (Fig. 1h), suggesting a lifting role in antigen-presenting control of adaptive immunity. ILCs also expressed increased inducible T-cell costimulatory (ICOS) levels (Fig. 1i), which promoted survival and cytokine production[20]. Moreover, neuropilin-1 (NRP-1) levels were elevated in fibrotic ILCs (Fig. 1j), supporting the notion that NRP-1-enhancing ILC activation mediated pulmonary fibrogenesis[19]. Decreased killer cell lectin-like receptor subfamily G member 1 (KLRG1) levels also suggested that ILCs in fibrotic lungs were newly expanded and activated (Fig. 1k). Some inhibitory molecules, including programmed cell death 1 (PD-1), programmed cell death-ligand 1 (PD-L1), and CD73 (Fig. 1l), but not T cell immunoglobulin and ITIM domain (TIGIT), lymphocyte-activation gene 3 (LAG3), or CD39, were augmented in ILCs from fibrotic lungs (Supplementary Fig. 1c), suggesting that activated ILCs negatively regulated the immune microenvironment. Remarkably, ILCs in silicotic lungs expressed decreased IL-13 but increased IFN-γ levels (Fig. 1m), which contradicted the notion that ILC2 was the dominant subset in lungs, thus indicating that ILC subsets in lungs were affected by CS particles. Collectively, these data indicated that ILCs in silicotic lungs were activated, while ILC subsets were affected by CS particles.

The ILC phenotype shifts from ILC2 to ILC1 in silicotic lungs

To gain insights into ILC changes concomitant with silicosis progression, we generated a mouse silicosis model with multiple end time points encompassing 8–10 and 12–14 weeks during fibrogenesis (Fig. 2a). We observed that a one-time CS particle treatment led to progressive pulmonary fibrosis. Silicotic pulmonary fibrosis became aggravated over time, which we monitored by Masson's and hematoxylin & eosin (H&E) staining (Fig. 2b and Supplementary Fig. 2a, b), and also western blotting to detect the ECM proteins fibronectin (FN) and collagen 1 (Col1) (Fig. 2c).

We next examined if silicosis progression was related to pulmonary ILC constitution. At a physiological state, $ST\text{-}2^+$ILC2s are dominant ILC components in the lungs. Strikingly, the ILC2 proportion decreased while $NKp46^+$ILC1 percentages gradually increased along with fibrosis progression (Fig. 2d and Supplementary Fig. 2c). To consolidate these findings, we examined expression of the fate-determining transcription factors T-bet and Gata-3 (Fig. 2e and Supplementary Fig. 2d). The results echoed our previous findings with the decreased IL-13 but increased IFN-γ on ILCs. The ILC1 to ILC2 ratio in silicotic lungs increased with silicosis progression. Furthermore, we used mice deficient in the recombination-activating gene 1 ($Rag1^{-/-}$), who lacked T and B cells but not ILCs, to establish a silicosis model (similar to C57BL/6J) (Fig. 2f) and observed that CS particles induced pulmonary fibrosis in these mice (Supplementary Fig. 2e). Intriguingly, shifted ILCs from group 2 to group 1 recurred in *Rag1*$^{-/-}$ mice, as manifested by cell surface marker and transcription factor expression (Fig. 2g, h and Supplementary Fig. 2f, g), thereby suggesting that the altered ILC2 to ILC1 ratio in silicosis progression was independent of adaptive immunity. Remarkably, the fibrotic degree in *Rag1*$^{-/-}$ mice was more severe than in C57BL/6J counterparts (Fig. 2i and Supplementary Fig. 2h), with more ECM deposition as previously reported[21]. Interestingly, pulmonary ILC1/ILC2 ratios were relatively higher in silicotic *Rag1*$^{-/-}$ mice than in C57BL/6J counterparts (Fig. 2j), suggesting that ratios were possibly linked to severe fibrosis. We also used another common pulmonary fibrosis model induced by bleomycin (BLM). Unlike treatment with CS, BLM-induced pulmonary fibrosis reverses at 3–5 weeks[22]. To induce persistent pulmonary fibrosis, we administered BLM twice and checked the pulmonary fibrosis degree in weeks 3 and 5 (Fig. 2k). Masson staining and western blotting for fibronectin and collagen 1 confirmed that BLM treatments led to progressive pulmonary fibrosis (Supplementary Fig. 2i, j). By checking NKp46 and ST-2 expression in ILCs, the same shift from ILC2s to ILC1s was observed (Fig. 2l), suggesting that ILC phenotypic changes were related to pulmonary fibrosis progression, but not specifically in silicosis.

We next explored why these ILCs had become altered. Significantly, decreased ILC2s were not due to cell death or egress into hilar lymph nodes (Supplementary Fig. 2k, l). Furthermore, using in vivo labeling, ILC alterations were unrelated to circulatory cell replenishment since circulating ILC1s were not increased in lungs (Supplementary Fig. 2m). Increased ILC1s were not attributed to cell

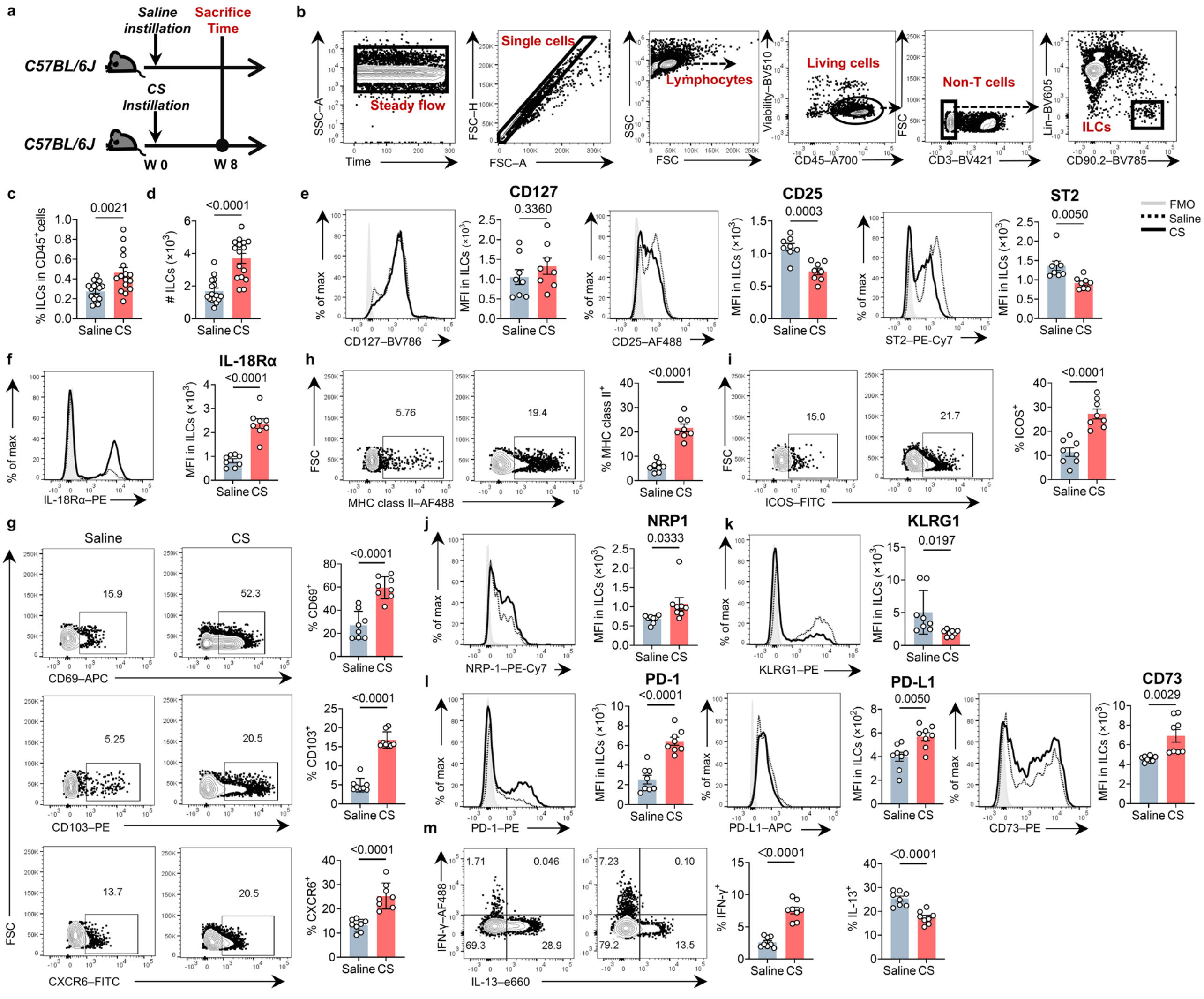

Fig. 1 | CS particles in lungs alter ILC phenotypes. a Experimental schematic showing mouse treatments and sacrifice time points. Week 8 post-CS treatment was regarded as the fibrogenesis stage. **b** The lung ILC gating strategy. Lineage (Lin) is an antibody cocktail containing CD5, CD45R (B220), CD11b, Ly-6B.2, Gr-1, and Ter-119. Bar graphs comparing ILC percentages (**c**) and cell numbers (**d**) in CS or saline-treated counterparts (*n* = 16 biological replicates). Flow histogram comparing ILCs expressing cytokine receptors, including CD127 (IL-7R), CD25 (IL-2Rα), ST-2 (IL-33R) (**e**), and IL-18Rα (**f**) in silicotic or saline-treated lungs. The bar graph compares the MFI of indicated cytokine receptors on ILCs (*n* = 8 biological replicates). **g** Flow plot showing the percentage of ILCs expressing the cell retention-related markers CD69, CD103, and CXCR6. Bar graphs compare indicated cell retention marker percentages on ILCs (*n* = 8 biological replicates). Flow plot showing ILCs expressing MHC-II (**h**) and ICOS (**i**) in fibrotic or saline-treated lungs. Bar graphs compare the percentage of ILCs expressing MHC- II (**h**) and ICOS (**i**) in silicotic or saline-treated lungs (*n* = 8 biological replicates). Flow histograms comparing ILCs expressing NRP-1 (**j**), KLRG1 (**k**), and PD-1, PD-L1, CD73 (**l**) in saline or CS-treated lungs. The bar graph compares the MFI of molecules on ILCs in lungs (*n* = 8 biological replicates). **m** Flow cytometric analysis of IFN-γ and IL-13 expression in ILCs from saline or CS-treated lung. Bar graphs compare IFN-γ and IL-13 percentages in ILCs (*n* = 8 biological replicates). FMO control, fluorescence minus one control. Bar graphs represent the combined results of four biologically independent experiments with similar results. Individual mice are plotted on graphs. Data are shown as the mean ± SEM. *P* values were calculated using two-tailed unpaired Student's *t*-tests and indicated in graphs. Source data are provided in a source data file.

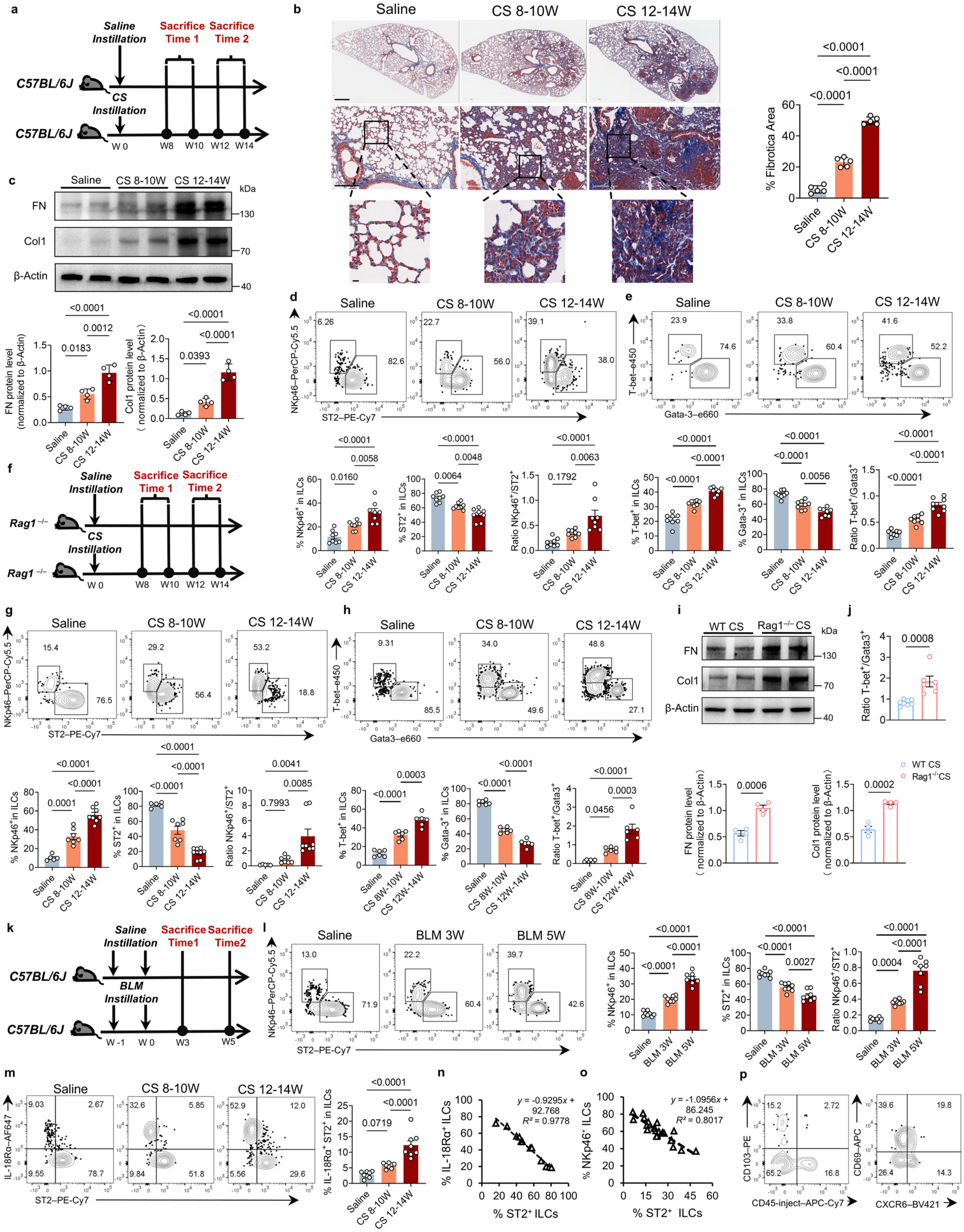

proliferation, as indicated by bromodeoxyuridine (BrdU) staining (Supplementary Fig. 2n). Next, bearing in mind elevated IL-18Rα expression in ILCs and its causal relationship to ILC1 function, we explored IL-18Rα expression in ILC subsets. NKp46$^+$ILC1s expressed high IL-18Rα levels, which increased concomitant with disease pathogenesis (Supplementary Fig. 2o). Interestingly, IL-18Rα$^+$ST-2$^+$ILC emergence in silicotic lungs, but not under physiological conditions, expanded with silicosis progression (Fig. 2m and Supplementary Fig. 2p). Increased IL-18Rα$^+$ILCs were not attributed to increased circulating ILCs (Supplementary Fig. 2q). Strikingly, ST2 loss on ILCs was strongly correlated with an increased parallel frequency of IL-18Rα$^+$ILCs and NKp46$^+$ILC1s (Fig. 2n, o). We further characterized IL-18Rα$^+$ST-2$^+$ILCs, which showed high expression of the tissue-retention markers CD69, CXCR6, and CD103, but few were labeled with

Fig. 2 | Pulmonary ILCs shift from ILC2 to ILC1s as silicosis progresses. **a** Experimental schematic. Saline or CS was administered to C57BL6J mice that were sacrificed at time 1: 8–10 weeks or time 2: 12–14 weeks post treatments. **b** Representative Masson's trichrome staining in lung section images showing whole lung lobes and zoomed in areas. Scale bar = 600 µm (upper panel), 200 µm (middle panels), and 50 µm (lower panels). The bar graph compares fibrotic area percentages in lung sections (*n* = 5 biological replicates). **c** Western blot showing fibronectin (FN) and collagen I (Col1) expression in CS-treated mouse lung groups. β-Actin was used as a loading control. Uncropped blots are in source data. The bar graph compares relative protein expression in lungs from different group (*n* = 4 biological replicates). **d** Flow plots showing NKp46$^+$ (ILC1) and ST-2$^+$ (ILC2) percentages in ILCs at indicated times. Bar graphs compare NKp46$^+$ and ST-2$^+$ percentages in ILCs and NKp46$^+$/ST-2$^+$ ILC ratios in lungs (*n* = 8 biological replicates). **e** Flow plots showing T-bet$^+$ and Gata-3$^+$ percentages in ILCs at indicated times. Bar graphs compare T-bet$^+$ and Gata-3$^+$ percentages in ILCs and T-bet$^+$/Gata-3$^+$ ILC ratios in lungs (*n* = 8 biological replicates). **f** Experimental schematic design: Saline or CS was administered to *Rag1*$^{-/-}$ mice that were sacrificed at indicated time points. **g** Flow plots showing NKp46$^+$ (ILC1) and ST-2$^+$ (ILC2) percentages in ILCs at indicated times. Bar graphs compare NKp46$^+$ and ST-2$^+$ percentages in ILCs and NKp46$^+$/ST-2$^+$ ILC ratios in lungs (*n* = 5 biological replicates in the saline group, *n* = 7 biological replicates CS 8-10 week, *n* = 8 biological replicates CS 12–14 weeks). **h** Flow plots showing T-bet$^+$ and Gata-3$^+$ percentages in ILCs at indicated time. Bar graphs compare T-bet$^+$ and Gata-3$^+$ percentages in ILCs and the T-bet$^+$/Gata-3$^+$ ratio in lungs (*n* = 6 biological replicates). **i** Western blot comparing fibronectin (FN) and collagen I (Col1) expressions in CS-treated C57BL/6 J and Rag1$^{-/-}$ mice lungs 12–14 weeks after CS treatment. β-Actin was used as a loading control. Uncropped blots are in source data. The bar graph compares relative protein expressions from different group (*n* = 4 biological replicates). **j** Bar graphs compare ratios of T-bet$^+$/Gata3$^+$ ILC in C57BL/6J and Rag1$^{-/-}$ mice lungs 12–14 weeks after CS treatment (*n* = 8 biological replicates in C57BL/6 group, *n* = 6 biological replicates in Rag1$^{-/-}$ group). **k** Schematic depicting bleomycin (BLM)-induced pulmonary fibrosis: BLM was administered to C57BL6J mice twice, at weeks 0 and 1. Mice were sacrificed at time 1: week 3 or time 2: week 5 post the last BLM treatment. **l** Flow plots showing NKp46$^+$ (ILC1) and ST-2$^+$ (ILC2) percentages in ILCs at indicated time points. Bar graphs compare NKp46$^+$ and ST-2$^+$ percentages in total ILCs and the NKp46$^+$/ST-2$^+$ ILC ratio in lungs (*n* = 8 biological replicates). **m** Flow plot showing ST-2 and IL-18Rα expression levels in ILCs from B6 mouse silicotic lungs. Bar graphs compare IL-18Rα$^+$ST-2$^+$ ILC percentages with silicosis progression (*n* = 8 biological replicates). Correlated ST2 and IL-18Rα expression (**n**) and correlated NKp46 and ST-2 expression levels (**o**) on ILCs from CS-treated B6 mice (*n* = 12 biological replicates). **p** Flow plots showing cell retention marker expression on IL-18Rα$^+$ST-2$^+$ ILCs in silicotic lungs at 12–14 weeks after CS treatment. Flow plots and bar graphs were representative of four biologically independent experiments with similar results. Individual mice are plotted on graphs. Data are shown as the mean ± SEM. *P* values were calculated using two-tailed unpaired Student's *t*-tests (two groups) or one-way ANOVA followed by Tukey's tests (three groups) and indicated on graphs. Source data are provided in a source data file.

circulating CD45 antibodies (Fig. 2p), suggesting that IL-18Rα$^+$ILC2s came from local ILC2 tissue pools. Collectively, these data indicated that major functional and phenotypic changes in lung resident ILCs occurred with silicosis progression, characterized by an ILC2 shift to ILC1s. However, why these ILC2/ILC1 shifts occurred remained unclear.

IL-18 mediates pulmonary ILC2 conversion to ILC1 in silicotic lungs

The strong negative correlation between ST2-expression and IL-18Rα$^+$ILCs, and also NKp46$^+$ILC1s in silicosis progression, suggested that ILC1s might emerge from local ILC2 pools. As ILCs can undergo plasticity in some circumstances[13], we performed cell transfer studies to explore whether ILC1s were converted from local ILC2s (Fig. 3a). We used congenic mice (CD45.1/2) and treated them intranasally with rIL-33, expanding lung ILC2s, which then underwent fluorescence-activated cell sorting (FACS) (Supplementary Fig. 3a). Sorted ILC2s were then transferred into *Rag1*$^{-/-}$ mice (CD45.2/2), who were in initial fibrogenesis stages (week 4). ILCs, readily identifiable by CD45.1 expression, infiltrated recipient *Rag1*$^{-/-}$ mouse lungs (Supplementary Fig. 3b). Sorted ILC2s were ST-2$^+$ and NKp46$^-$ labeled, and were converted to a NKp46$^+$ST-2$^-$ phenotype which expressed high IL-18Rα levels (Fig. 3b), implying a critical role for IL-18 signaling in ILC conversion. We further examined transcription factor expression in transferred ILCs; significantly, ILC2s downregulated ST-2 and correlated with striking upregulation of T-bet, an ILC1-specific transcription factor. Also, converted ILCs expressed high IL-18Rα levels but downregulated Gata-3 (Fig. 3c). Collectively, these data indicated that ILC2s converted to ILC1s in line with silicosis progression.

To consolidate ILC conversion data, we generated ST-2-eGFP reporter mice by inserting *eGFP* into exon2 of *Il1rl1* (encodes ST2, a direct target of *Gata3*, and commonly used to label ILC2s), in which eGFP$^+$ILCs were *bonafide* ILC2s (Fig. 3d). We also identified ST2(eGFP)$^+$ cells which were almost exclusively labeled with ST2 fluorescent antibodies, which decreased as silicosis progressed (Supplementary Fig. 3c). In examining IL-18Rα expression on ILCs in ST2-eGFP mice, we observed that it emerged on eGFP$^+$ cells. Notably, a significant leaning shift was identified from ST-2(eGFP)$^+$ to IL-18Rα$^+$ILCs (Fig. 3e), meaning ILC2 conversion to ILC1s. Apparently, the Mean Fluorescence Intensity (MFI) of IL-18Rα expression on ST-2(eGFP)$^+$IL-18Rα$^+$ILCs was lower than that on ST2(eGFP)$^-$IL-18Rα$^+$ILCs (Fig. 3f). We also investigated the IL-12 receptor which was reportedly related to ILC conversion[14,17], but few ILCs expressed IL-12Rβ2 (Supplementary Fig. 3d), suggesting a weak relationship with ILC conversion in silicotic lungs.

To examine if IL-18 receptor signaling mediated ILC conversion in silicosis progression, we treated fibrotic mice with IL-18Rα blocking antibodies (Fig. 3g). Using flow cytometry, ILC1/ILC2 ratios in lungs were reduced by blocking treatment (Fig. 3h), suggesting that IL-18 receptor signaling was critical for ILC conversion. Moreover, blocking IL-18 receptor signaling attenuated CS-induced pulmonary fibrosis (Fig. 3i and Supplementary Fig. 3e). Furthermore, we also established silicosis model with IL-18 knockout (KO) mice (*Il18*$^{-/-}$), established silicosis model. We examined ILC ratios during silicosis progression and found that ILC1 and ILC2 ratios were comparable between wild-type and *Il18*$^{-/-}$ mice under physiological conditions. Mice deficient in IL-18 generated decreased ILC1/ILC2 ratios as silicosis progressed, at both 8-10 and 12–14 weeks (Fig. 3j). Accordingly, less ECM was deposited in *Il18*$^{-/-}$ mouse lungs (Fig. 3k and Supplementary Fig. 3f).

To ultimately verify our hypothesis that IL-18 mediated ILC conversion in silicosis progression, we repeated ILC2 transfer studies, but recipient mice were replaced with *Rag1*$^{-/-}$*Il18*$^{-/-}$ double KO (dKO) mice (Fig. 3l). Flow cytometry demonstrated that transferred ILC2s were not converted to ILC1s in the dKO mice (Fig. 3m). T-bet expression in transferred ILCs was quite low in the dKO (Fig. 3n), suggesting that IL-18 was critical for ILC2 conversion to ILC1 during silicosis.

Thus, ILC1s in fibrotic lungs were derived from local ILC2 pools rather than existing ILC1 outgrowth, mediated by IL-18. However, IL-18 cellular origins required investigation.

Mechanics-activated fibroblasts secrete IL-18 and modulate ILC2 conversion to ILC1

It is hypothesized that IL-18 is tightly linked to pyroptotic macrophages which may regulate ILC conversion. To test this, we used clodronate liposomes (CL) to deplete macrophages during silicosis progression, from week 7–12 post-CS treatment (Fig. 4a). CL treatment effectively depleted interstitial macrophages (IMs) and alveolar macrophages (AMs) in silicotic lungs (Supplementary Fig. 4a). Intriguingly, the fibrotic degree was not significantly affected by CL treatment (Supplementary Fig. 4b, c). Also, the depletion did not significantly alter ILC1/ILC2 ratios in lungs (Fig. 4b), suggesting that macrophage-derived IL-18 had limited roles in ILC conversion during fibrogenesis. Different IL-18 sources have been identified, including leukocytes and stromal cells[23]. To further investigate whether leukocyte-derived IL-18

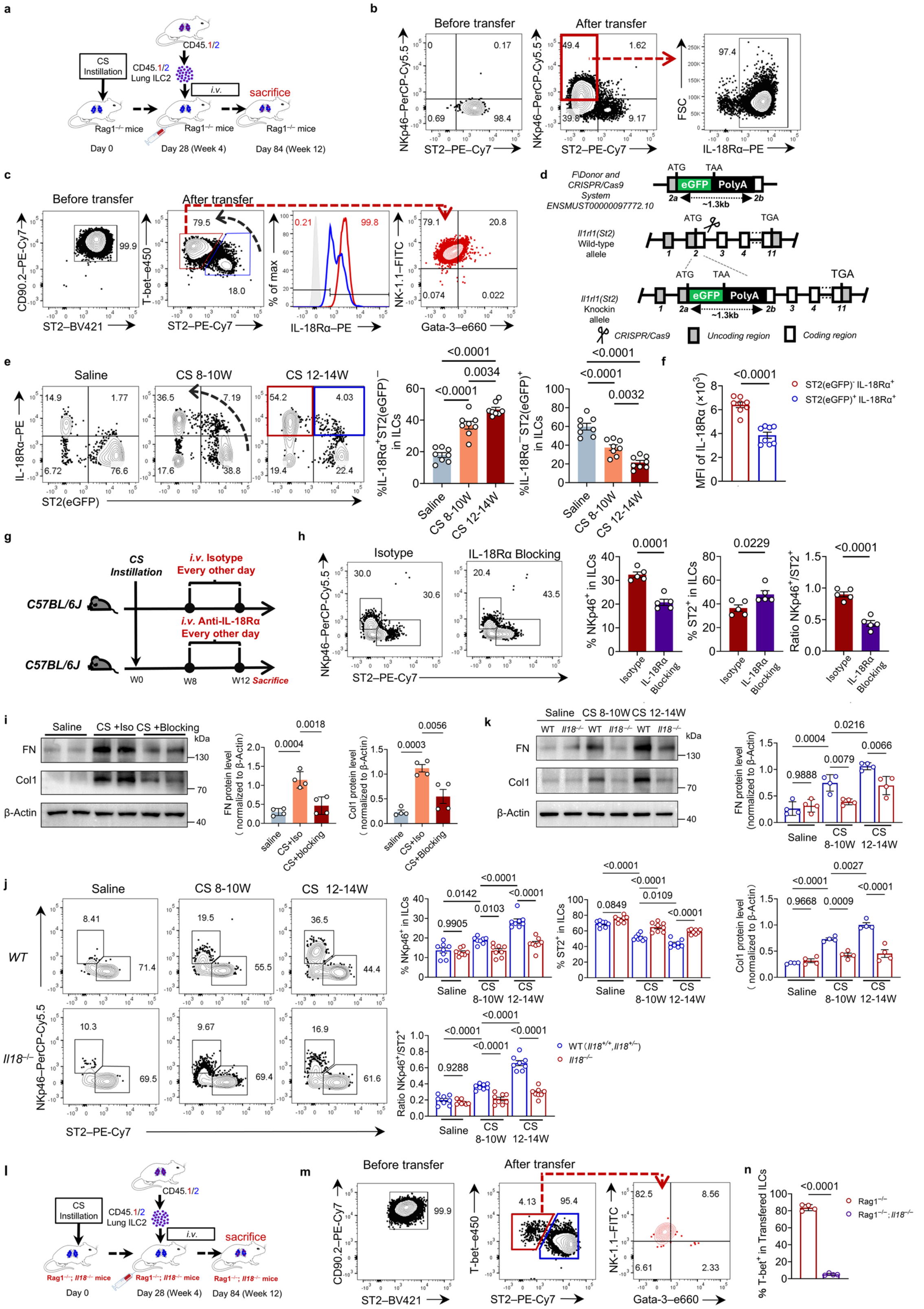

regulated ILC conversion, we constructed bone marrow (BM) chimaera mice using wild-type and $Il18^{-/-}$ BM cells that was transferred to wild-type mice, which were further established with silicosis model (Fig. 4c). Flow cytometry was then used to detect ILC ratios in lungs. We observed that hematopoietic cells lacking IL-18 did not significantly boost ILC1s in CS-injured lungs, but ILC2 percentages were decreased, which increased ILC1/ILC2 ratios in hematopoietic cells lacking IL-18 (Fig. 4d). These results indicated that it was not IL-18 from leukocytes, but IL-18 from non-hematopoietic stromal cells that was required for ILC conversion. To explore the IL-18 cell source that putatively mediated ILC conversion, we examined ILC1 and ILC2 dynamic changes in lungs from inflammatory (second and fourth week after CS treatment) to fibrogenesis stages (8–10 and 12–14 weeks after CS treatment). Although ILC1s percentages increased at inflammatory stages (second

Fig. 3 | IL-18 mediates ILC2 conversion to ILC1s in silicotic lungs. a Experimental schematic showing the ILC2 transfer experimental design. Details are described in methods. **b** Flow plot analyzing ST-2 and NKp46 expression on donor ILC2s before and after transfer. IL-18Rα levels were then analyzed on ST-2^{-}NKp46^{+} ILCs ($n = 6$ biological replicates). **c** Flow plot showing transcription factor T-bet and Gata3 expression on donor ILC2s before and after transfer. The flow histogram compares IL-18Rα on ST-2^{+}T-bet^{-} (blue) and ST-2^{-}T-bet^{+} ILCs (red). NK-1.1 and Gata-3 expression was analyzed on ST-2^{-}T-bet^{+} transferred ILCs ($n = 4$ biological replicates). **d** Schematic showing ST2-eGFP reporter construction. Details are provided in methods. **e** Flow plots showing ILC2 (eGFP^{+}) and non-ILC2 (eGFP^{-}) percentages expressing IL-18Rα concomitant with silicosis progression ($n = 8$ biological replicates). **f** Bar graph compares MFI values for IL-18Rα in (eGFP^{+})IL-18Rα^{+} ILC2s and (eGFP^{-})IL-18Rα^{+} non-ILC2s ($n = 8$ biological replicates). **g** Schematic showing the IL-18Rα blocking experiment: silicotic B6 mice were blocked with IL-18Rα or treated with isotype-matched antibodies. Details are described in methods. **h** Flow plots showing NKp46^{+} (ILC1) and ST-2^{+} (ILC2) percentages in pulmonary ILCs. Bar graphs compare NKp46^{+} and ST-2^{+} percentages in ILCs and the NKp46^{+}/ST-2^{+} ILC ratio in lungs ($n = 5$ biological replicates). **i** Western blot shows FN and Col1 levels in lungs. Uncropped blots are in source data. Bar graph compares relative protein levels across different lung treatments ($n = 4$ biological replicates). **j** Flow plots showing NKp46^{+} (ILC1) and ST-2^{+} (ILC2) percentages in pulmonary wild-type and *Il18*$^{-/-}$ littermate silicotic ILCs at different times. Bar graphs compare NKp46^{+} (ILC1) and ST-2^{+} (ILC2) ILC percentages and ILC1/ILC2 ratios in silicotic lungs ($n = 8$ biological replicates). **k** Western blot shows FN and Col1 levels in wild-type and *Il18*$^{-/-}$ mouse lungs. Uncropped blots are in source data. The bar graph compares relative protein levels in lungs ($n = 4$ biological replicates). Littermate mice were used in (**j**), (**k**). **l** Schematic showing the ILC2 transfer experimental design; recipients were *Rag1*$^{-/-}$*Il18*$^{-/-}$ dKO mice. **m** Flow plot showing ST-2, NKp46, T-bet, and Gata-3 expression on donor ILC2s before and after transfer. **n** Bar graph comparing T-bet percentages in transferred ILCs in different recipients ($n = 4$ biological replicates). Bar graphs represent the combined results of four biologically independent experiments with similar results. Individual mice are plotted on graphs. Data are shown as the mean ± SEM. *P* values were calculated using two-tailed unpaired Student's *t*-tests (**f**, **h**, **n**) or one-way ANOVA followed by Tukey's tests (**e**, **i**, **j**, **k**). *P* values are indicated on graphs. Source data are provided in a source data file. Mouse figures in panel (**a**) and (**l**) were created in BioRender. Fan, Y. (2024) BioRender.com/u22s346.

and fourth weeks), ILC1/ILC2 ratios surged at 12–14 weeks (the fibrotic stage) indicating that ILC2 conversion to ILC1 was related to fibrogenesis (Supplementary Fig. 4d).

As fibroblasts actively proliferate during fibrosis and secrete cytokines which modulate the immune microenvironment, we hypothesized that fibroblasts might control ILC conversion. From immunofluorescence (IF) confocal images, ILC2s (Lin^{-}Gata-3^{+}) were clustered around or interacted with activated fibroblasts (α-SMA^{+} staining) (Fig. 4e), implying that fibroblasts modulated ILC conversion. Furthermore, we examined whether activated fibroblasts (secreting IL-18) in an in vitro matrix stiffness-activated fibroblast model mimicked fibroblast activation in silicotic lungs and avoided exogenous cytokine effects (Supplementary Fig. 4e). Notably, stiff matrix-cultured fibroblasts generated a sharp increase in pro-IL-18 levels (Fig. 4f). We also observed that the stiff matrix activated caspase 1 (converts pro-IL-18 to its mature form) in fibroblasts was manifested by increased MFI of FLICA (Fig. 4g). Accordingly, mature IL-18 was also increased in cell culture medium (CM) (Fig. 4h). These data demonstrated that high mechanics-activated fibroblasts secreted IL-18, dependent on caspase 1 activity, may modulate ILC conversion.

To directly verify that activated fibroblasts modulated ILC2 conversion to ILC1, we performed in vitro studies. First, we cultured sorted pulmonary ILC2s with CM from different stiffness-treated fibroblasts (Fig. 4i). A high proportion of NK1.1^{+} ILCs was detected in ST-2^{+}ILC2s cultured with CM from high stiff-activated fibroblasts, while the ST-2^{+}NK1.1^{-} ratio was decreased (Fig. 4j). ST-2^{+}NK1.1^{+} ILCs increased, suggesting that the CM may have mediated ILC conversion. To consolidate these findings, we generated a transwell fibroblast/ILC2 co-culture system, where fibroblasts continuously produced IL-18 (Fig. 4k). After 36 h of co-culture, we observed a lift ratio of NKp46^{+}ILC1s and decreased ST-2^{+}ILC2s, analogous to CM-cultured ILC2s (Supplementary Fig. 4g, h). Strikingly, when co-culturing continued for 60 h, a boosted NKp46^{+}ILC1 ratio was observed (Fig. 4l), indicating that activated fibroblasts modulated ILC conversion in a time-dependent manner. To verify that fibroblast-derived IL-18 modulated ILC2 conversion, we repeated co-culturing with primary fibroblasts isolated from *Il18*$^{-/-}$ mice (Fig. 4m). Conclusively, while stimulated by the high stiff gel, fibroblasts lacking IL-18 did not lead to ILC2 conversion (Fig. 4n). As some reports have indicated that ILC1s secrete matrix metalloproteinase 9 (MMP9) and transforming growth factor β1 (TGF-β) to promote fibrosis[24,25], we performed qPCR on ILCs in upper chambers. Activated fibroblasts mediated ILC conversion and upregulated *Mmp9* and *Tgfb1* transcripts (Fig. 4o), which potentially mirrored converted ILC1 functions in fibrogenesis. Furthermore, we examined if high mechanics activated ILC2s directly and affected fibroblast proliferation. So, we changed fibroblast and ILC2 positions in chambers and wells (Supplementary Fig. 4i). Our results excluded the possibility that mechanics could mediate ILC2 conversion directly, further affecting fibroblast proliferation in vitro (Supplementary Fig. 4j, k). Collectively, these data demonstrated that IL-18 derived from mechanics-activated fibroblasts modulated ILC2 conversion to ILC1, but the molecular mechanisms remained unclear.

Mechanics-activated fibroblasts secrete IL-18 which is dependent on Notch3 signaling

To understand the molecular mechanism underpinning fibroblast-mediated ILC conversion, we performed bulk RNA-sequencing on primary lung fibroblasts cultured on matrix gels, and identified upregulated and downregulated transcripts, respectively, in stiff matrix-cultured fibroblasts (Fig. 5a). First, Gene ontology (GO) analysis showed that more upregulated genes were enriched in inflammatory response and wound healing processes, implying critical mechanics-activated fibroblast roles in immune-regulation and fibrogenesis (Fig. 5b). Besides, the positive regulation of focal adhesion assembly, inflammatory response, chemotaxis, and angiogenesis were all involved in the process of fibrogenesis (Fig. 5b). Further, we did Kyoto Encyclopedia of Genes and Genomes (KEGG) analysis and several signaling pathways were enriched in the activated fibroblasts (Fig. 5c). HIF-1 signaling pathway, PI3K-Akt signaling pathway, Complement and coagulation cascades were contributed to the development of fibrosis[26–28]. While rheumatoid arthritis and Coronavirus disease–COVID-19 related signaling guided the onset of fibrosis[29,30]. Besides, ECM-receptor interaction that related to mechanical sensing were enriched. Furthermore, Cytokine-cytokine receptor interaction, IL-17 signaling pathway that related to cytokine secretion and immune regulation were also covered (Fig. 5c). The enriched signaling pathways supported that fibroblasts would be affected by mechanics, secreting cytokines, and promoting the progression of fibrosis.

To gain more insights, we used the STRING database to predict protein–protein interactions. The top 1018 hits revealed potential protein–protein interaction modules, including adherens junction, TGF-β, TNF, toll-like receptor signaling, and cytokine–cytokine receptor interactions (Fig. 5d). From further examination of these modules, a central interaction network was identified; Notch signaling (Fig. 5d). Among Notch receptors, Notch3 is the sole upregulated receptor in fibroblasts in human fibrotic lungs[31]. Importantly, the receptor is also reportedly linked to HIF-1 and PI3K-Akt signaling[32–35]. Given that Notch3 signaling in fibroblasts may be a mediator in some diseases, including fibrogenesis[36] and RA[37] (both predicted in GO and KEGG analysis), Notch3 signaling was a putative candidate implicated in ILC conversion.

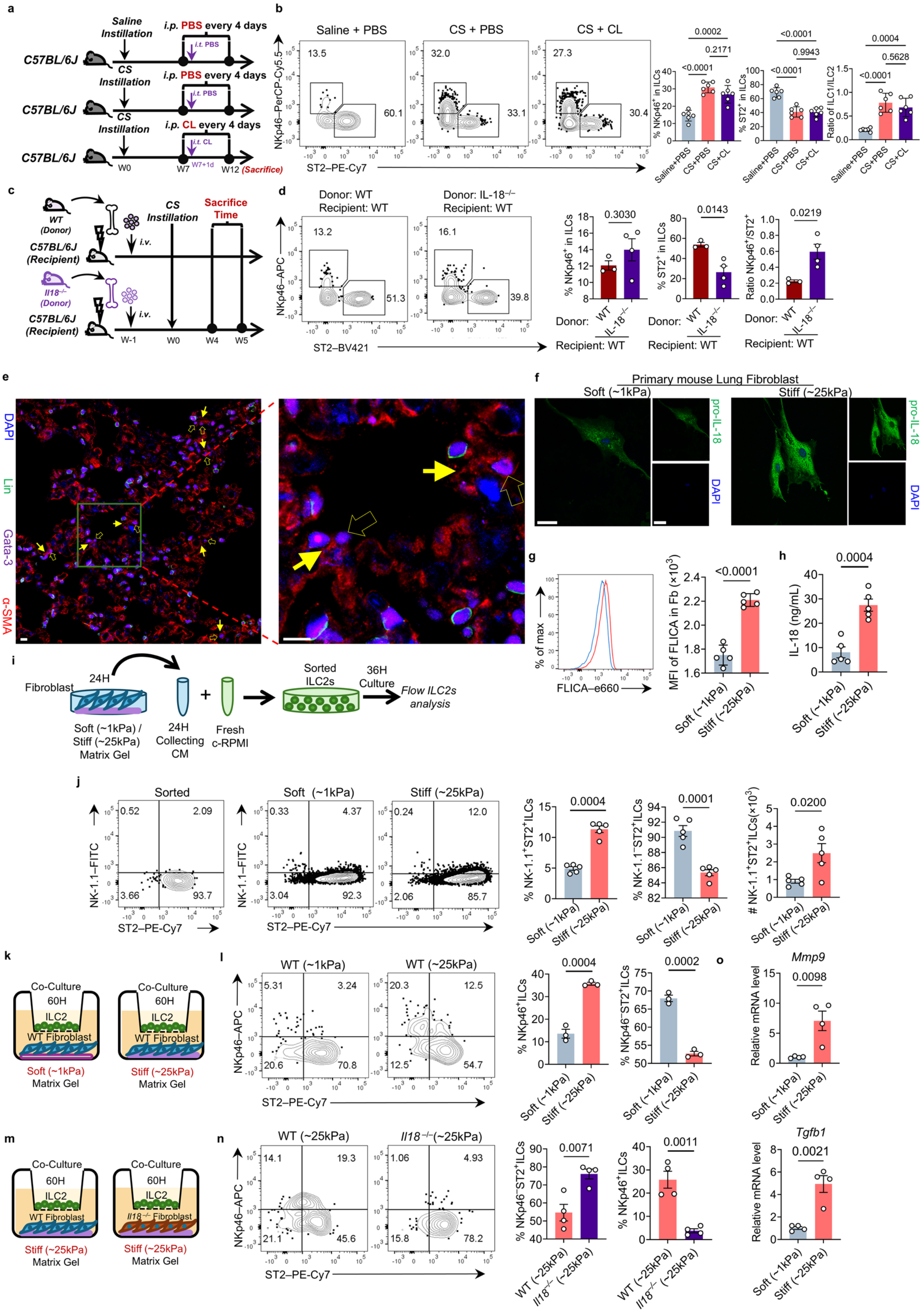

To explore Notch3 roles in activated fibroblasts, we performed western blotting and observed sharply increased Notch3 intracellular domain (Notch3ICD, the active domain of Notch3) expression in activated fibroblast nuclei (Fig. 5e). Consistently, increased nuclear Notch3ICD localization was observed in both activated primary fibroblasts and the fibroblast cell line MLg2908, confirming that high mechanics activated Notch3 signaling in fibroblasts (Fig. 5f). To directly explore the relationships between Notch3 and IL-18 expression in fibroblasts, we generated fibroblast-specific *Notch3* KO mice by crossing Notch3$^{fl/fl}$ mice with Col1a2-creERT mice (Fig. 5g and Supplementary Fig. 5a). *Notch3* was effectively knocked down in isolated primary fibroblasts (Supplementary Fig. 5b). We then isolated these

Fig. 4 | Mechanics-activated fibroblasts secrete IL-18 which modulates ILC2 conversion to ILC1s. **a** Schematic showing the macrophage deletion experiment: Clodronate liposomes (CL) were intraperitoneally (*i.p*) injected into mice to delete IMs or, *i.t.* instilled to delete AMs. Treatment details are in methods. **b** Flow plots showing NKp46$^+$ (ILC1) and ST-2$^+$ (ILC2) percentages in pulmonary ILCs. Bar graphs compare NKp46$^+$ and ST-2$^+$ percentages in ILCs and the NKp46$^+$/ST-2$^+$ ILC ratio in lungs of mice in different treatment groups ($n = 6$ biological replicates). **c** Schematic showing the construction of bone-marrow chimeric mice. Treatment details are in methods. **d** Flow plots showing NKp46$^+$ (ILC1) and ST-2$^+$ (ILC2) percentages in pulmonary ILCs. Bar graphs compare NKp46$^+$ and ST-2$^+$ percentages in ILCs and the NKp46$^+$/ST-2$^+$ ratio in lungs ($n = 3$ biological replicates wild-type→wild-type, $n = 4$ biological replicates *Il18*$^{-/-}$→wild-type). **e** Confocal immunofluorescence images showing lungs in silicosis mice. DAPI (blue), Lineage (green), Gata-3 (purple), and α-SMA (red) labeling. Solid arrows indicate fibroblasts and hollow arrows indicate ILC2s. Scale bar = 5 μm (left panel), 20 μm (right panel). (Representative image from 4 biological independent replicates with similar results). **f** Immunofluorescence images showing pro-IL-18 staining in primary lung fibroblasts cultured on soft (~1 kPa) or stiff (~25 kPa) matrix gels, Scale bar = 20 μm (Representative image from 6 independent cultures with similar results). **g** Flow histogram showing caspase 1 activity (FLICA) of primary lung fibroblasts cultured on soft (~1 kPa) and stiff (~25 kPa) matrix gels. The bar graph compares fibroblast FLICA MFI values in different groups ($n = 5$ biological replicates). **h** IL-18 levels in primary lung fibroblast culture medium (CM) on soft (~1 kPa) or stiff (~25 kPa) matrix gels were detected by ELISA ($n = 5$ biological replicates). **i** Schematics showing sorted ILC2s cultured in fibroblast CM. See methods for details. **j** Flow plots showing NK1.1 and ST-2$^+$ expression in ILC2s cultured on soft (~1 kPa) or stiff (~25 kPa) matrix gels. Bar graphs compare NK1.1$^+$ST-2$^+$ and NK1.1$^-$ST-2$^+$ ILC percentages and the number of NK1.1$^+$ST-2$^+$ cells ($n = 5$ biological replicates). **k** Schematic showing the primary lung fibroblast and sorted lung ILC2 co-culturing system used in (**l**). See methods for details. **l** Flow cytometry data showing NKp46 and ST-2 expression of upper-chamber ILC2s which were co-cultured with lower-chamber primary lung fibroblast on soft (~1 kPa) or stiff (~25 kPa) matrix gels for 60 h ($n = 3$ biological replicates). **m** Schematic showing the primary lung fibroblast and sorted lung ILC2 co-culturing system used in (**n**). **n** Flow cytometry data showing NKp46 and ST-2 expression of upper-chamber ILC2s which were co-cultured with lower-chamber wildtype or *Il18*$^{-/-}$ primary lung fibroblast on stiff (~25 kPa) matrix gels for 60 h ($n = 4$ biological replicates). **o** qPCR analysis of *Mmp9* and *Tgfb1* transcripts in upper-chamber ILC2s which were co-cultured with lower-chamber primary lung fibroblast on soft (~1 kPa) or stiff (~25 kPa) matrix gels for 60 h ($n = 4$ biological replicates). Bar graphs represent the combined results from three biologically independent experiments with similar results. Individual values are plotted in graphs. Data are shown as the mean ± SEM. *P* values were calculated using two-tailed unpaired Student's *t*-tests (**d**, **g**, **h**, **j**, **l**, **n**) or one-way ANOVA followed by Tukey's tests (**b**) and are indicated in graphs. Source data are provided in a source data file.

pulmonary fibroblasts and repeated previous in vitro studies. IF staining showed that Notch3 abrogated decreased pro-IL-18 expression in stiff matrix-activated fibroblasts (Fig. 5h). Notably, caspase 1 activity in *Notch3* KO fibroblasts was also decreased, though stimulated by high stiff mechanics (Fig. 5i). Accordingly, the bioactive IL-18 form in *Notch3*-abrogated fibroblast CM was reduced (Fig. 5j). Therefore, Notch3 signaling was required for the mechanics-activated fibroblast secretion of IL-18 via caspase 1.

Notch3 signaling in fibroblasts mediates ILC conversion associated with attenuated fibrotic phenotypes

As Notch3 mediated IL-18 production in mechanics-activated fibroblasts in vitro, we next explored if it modulated ILC conversion in vivo and examined its effects on CS-induced pulmonary fibrosis. Consistent with previous observations, upregulated Notch3 expression occurred in activated fibroblasts from silicotic lungs (Fig. 6a). Furthermore, we used fibroblast-specific *Notch3* KO mice and tamoxifen (TAM) treatment to disrupt Notch3 signaling in fibroblasts at specific times. First, TAM was applied from week 3–4 after CS treatment, when relays of acute inflammation and fibrogenesis (Fig. 6b). Under physiological conditions, *Notch3* KO in fibroblasts did not alter ILC ratios. We also prospectively analyzed ILC1/ILC2 ratios in fibrotic lungs at 8–10 weeks but did not identify significantly altered ratios (Fig. 6c). Unexpectedly, during fibrosis progression at weeks 12–14, ILC1/ILC2 ratios were decreased in *Notch3* KO mice (Fig. 6c and Supplementary Fig. 6a), demonstrating fibroblasts would affect ILC conversion dependent on Notch3 at the fibrotic stage of silicosis.

We also explored whether reduced ILC conversion was linked to attenuated fibrotic phenotypes. Histology (Masson's and H&E staining) indicated that Notch3$^{fl/fl}$Colla2-Cre mice, with reduced ILC1/ILC2 ratios at 12–14 weeks, showed relatively attenuated collagen deposition and cellular nodules (Fig. 6d and Supplementary Fig. 6b), demonstrating that Notch3 signaling in fibroblasts controlled ILC conversion and also fibrogenesis. However, in mice with unaffected ILC ratios (weeks 8–10), no alleviated fibrogenesis was observed. To confirm this attenuated fibrosis at 12–14 weeks, we examined ECM protein expression (fibronectin and collagen 1) in lung tissues, which echoed previous Masson's staining (Fig. 6e). Furthermore, as hydroxyproline is the sole confirmed marker for quantifying lung fibrosis, we examined its content in lungs (Fig. 6f). The results were similar to ECM protein expression levels by western blotting, thus verifying that Notch3 signaling in fibroblasts modulated ILC conversion, as well as the degree of fibrogenesis. Furthermore, by monitoring tidal volume (TV) and breathing frequency (f) in silicotic mice, we extended our conclusion that the attenuated fibrosis phenotype with fast recovered pulmonary functions (Supplementary Fig. 6c). The protection conferred by a lack of Notch3 signaling in fibroblasts in lungs showed not only a more preserved morphology but provided a better assessment of pulmonary function.

Next, in accepting that fibroblasts actively proliferate in fibrogenesis, we applied TAM at fibrosis progression stages (weeks 7–8) after CS treatment, to examine Notch3 actions in fibroblasts at fibrogenesis stages (Fig. 6g). From ILC flow cytometry, we observed restored ILC2 proportions, while ILC percentages were not appreciably impacted by Notch3 ablation in this period. The ILC1/ILC2 ratio was not significantly affected (Fig. 6h and Supplementary Fig. 6d). Additionally, Masson's staining demonstrated that abrogating Notch3 at this stage did not affect fibrogenesis (Supplementary Fig. 6e). Collectively, these results indicated that Notch3 signaling in fibroblasts was essential for ILC conversion in silicosis, but in a time-dependent manner.

We also used a BLM-induced pulmonary fibrosis model to explore whether Notch3 actions in fibroblasts were restricted to silicosis. As shown, mice received repeated BLM treatments, and TAM was applied at inflammatory stages (weeks 1–2) post-BLM treatment (Fig. 6i). Using Masson's and H&E staining, mice with abrogated Notch3 in fibroblasts showed relatively mild fibrosis (Supplementary Fig. 6f). We also examined ILC percentages and pulmonary ILC1/ILC2 ratios at week 5 after the last BLM treatment. We observed reduced ILC1s and restored ILC2s in lungs, and a decreased ILC1/ILC2 ratio, in accordance with alleviated phenotypes in pulmonary fibrosis (Fig. 6j and Supplementary Fig. 6g). These results showed that a lack of Notch3 signaling in fibroblasts conferred protective effects in lungs against fibrogenesis, which was not restricted to silicosis. Taken together, our data indicated that Notch3 signaling in fibroblasts controlled ILC2 conversion to ILC1 in fibrotic lungs, which was linked to the fibrogenesis degree.

Discussion

Tissue-resident ILCs are critical for regulating tissue homeostasis and inflammatory responses. We investigated pulmonary ILC phenotypes in silicotic mice and unexpectedly discovered reduced ILC2s and expanded ILC1s, concomitant with silicosis progression, further verifying a conversion in ILC subsets, mediated by IL-18. Also, ILC conversions were modulated by activated fibroblasts. Similarly, loss of Notch3 (mechanosensitive receptor) in fibroblasts, parallel to blocking

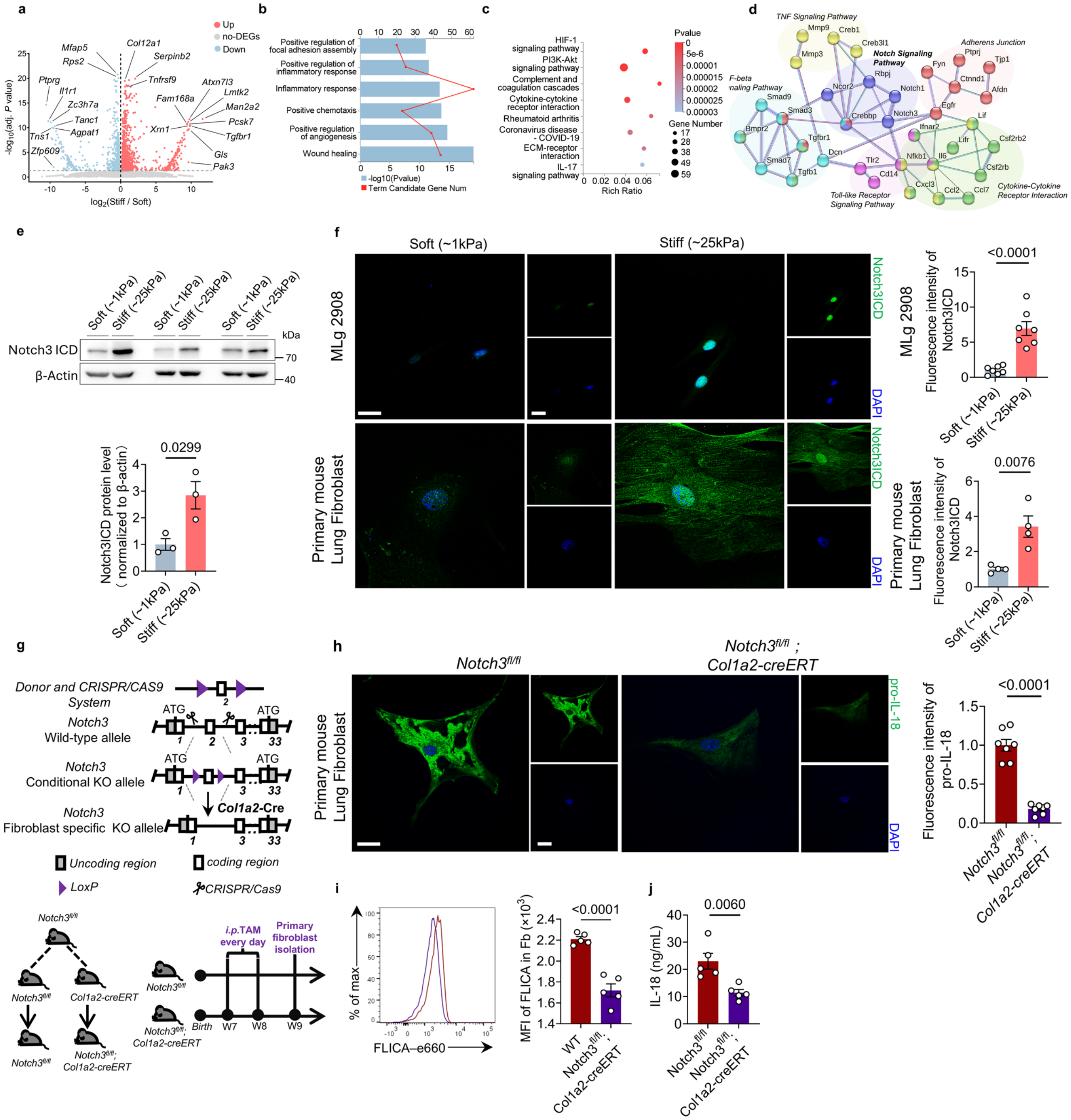

Fig. 5 | Notch3 signaling is essential for IL-18 expression in mechanics-activated fibroblasts. a Volcano plot of differentially expressed genes in bulk RNA-Sequencing dataset of soft (~1 kPa) or stiff (~25 kPa) gel cultured fibroblasts. Upregulated genes and downregulated genes are highlighted in red and blue ($n = 3$ biological replicates). **b** GO analysis of upregulated genes in stiff gel cultured fibroblasts predicts the involved biological processes. **c** KEGG enrichment analysis of upregulated genes. **d** Bioinformatics analysis of the protein–protein interaction network using STRING. **e** Western blot showing Notch3 intracellular domain (ICD) expression in primary lung fibroblasts cultured on different stiffness matrix gels. Uncropped blots are in source data. The bar graph compares Notch3 intracellular domain (ICD) expression in soft (~1 kPa) or stiff (~25 kPa) gel cultured fibroblasts ($n = 3$ biological replicates). **f** Immunofluorescence images showing Notch3 ICD staining in MLg2908 and primary lung fibroblasts cultured on soft (~1 kPa) or stiff (~25 kPa) matrix gels. DAPI was used to label nuclei. Scale bar = 20 µm. Bar graphs compare Notch3 ICD fluorescence intensities ($n = 7$ biological replicates, MLg2908; $n = 4$ biological replicates, primary fibroblasts). **g** Schematic showing Notch3 flox mouse construction, and the breeding strategy for fibroblast-specific *Notch3* depletion mice. Lung primary fibroblasts were then isolated for in vitro experiments. **h** Immunofluorescence images showing pro-IL-18 staining in primary lung fibroblasts isolated from *Notch3*$^{fl/fl}$ and *Notch3*$^{fl/fl}$ *Col1a2*-creERT littermates cultured on stiff (~25 kPa) matrix gel. Scale bar = 20 µm. The bar graph compares pro-IL-18 fluorescence intensity of *Notch3*$^{fl/fl}$ and *Notch3*$^{fl/fl}$ *Col1a2*-creERT primary lung fibroblasts cultured on stiff (~25 kPa) matrix gel ($n = 7$ biological replicates). **i** Flow histogram showing primary lung fibroblast caspase 1 activity (FLICA). The bar graph compares FLICA MFI values in *Notch3*$^{fl/fl}$ and *Notch3*$^{fl/fl}$ *Col1a2*-creERT primary lung fibroblasts cultured on stiff (~25 kPa) matrix gel. ($n = 5$ biological replicates). **j** Bar graph comparing IL-18 levels in culture medium from stiff (~25 kPa) matrix gel stimulated primary lung fibroblasts isolated from *Notch3*$^{fl/fl}$ and *Notch3*$^{fl/fl}$ *Col1a2*-creERT littermates as detected by ELISA ($n = 5$ biological replicates). Bar graphs represent the combined results of three biologically independent experiments with similar results. Individual values are plotted in graphs. Data are shown as the mean ± SEM. *P* values were calculated using two-tailed unpaired Student's *t*-tests and are indicated in graphs. Source data are provided in a source data file.

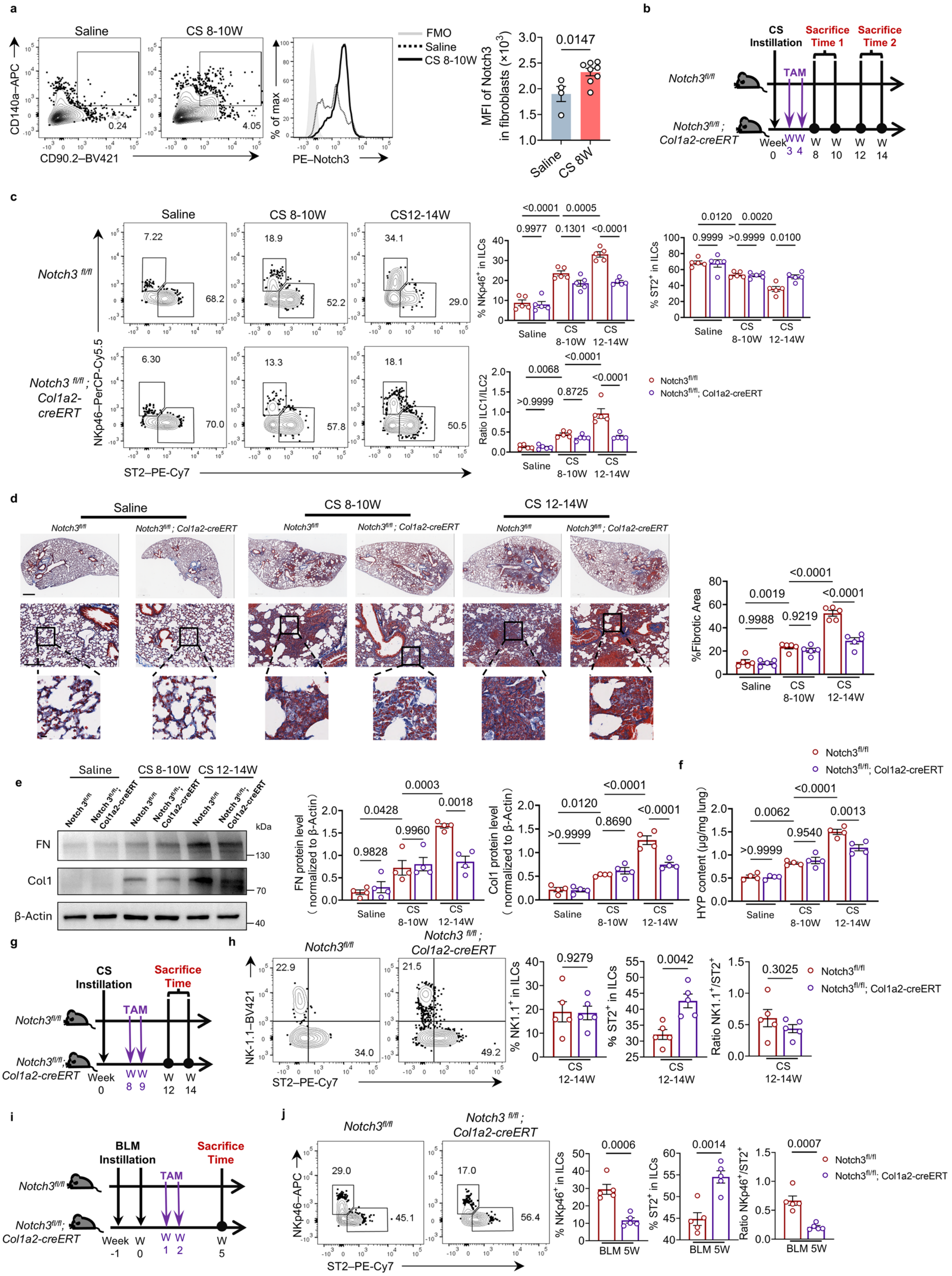

ILC remodeling, also impeded fibrosis progression, suggesting that Notch3 may be a promising therapeutic target for silicosis. These data expanded our knowledge of fibroblasts as both crucial effector cells in fibrogenesis and immune regulators in local immune homeostasis (Fig. 7).

We used $Rag1^{-/-}$ mice to establish a mouse silicosis model and demonstrated that CS-induced pulmonary fibrosis developed independent of adaptive immunity. This observation was first proposed by Beamer and colleagues[21], when the ILC concept had not been formulated. Recently, several research groups have investigated ILC roles in different disease pathologies using Thy1.2 antibodies. However, ILC actions in silicosis pathogenesis remain elusive. In addressing this knowledge gap, we unexpectedly discovered ILC2 conversion to ILC1s in silicosis. While we did not explore the functional effects of

Fig. 6 | Notch3 signaling in fibroblasts mediates ILC2 conversion to ILC1s, and is associated with an attenuated fibrotic phenotype. **a** Flow plot showing fibroblasts ($CD45^-CD140a^+CD90.2^+$) in CS-treated lungs. Flow histogram and bar graph compare Notch3 MFI values in fibroblasts from saline or CS-treated lungs (saline, *n* = 4 biological replicates; CS 8–10 weeks, *n* = 8 biological replicates). **b** Schematic showing tamoxifen (TAM)-induced fibroblast-specific *Notch3* depletion. TAM was applied at early fibrogenesis stages (week 3–4 after CS treatment). **c** Flow plots showing $NKp46^+$(ILC1) and $ST\text{-}2^+$(ILC2) percentages in lungs (*n* = 5 biological replicates). Bar graphs compare ILC2 and ILC1 percentages in ILCs and ILC1/ILC2 ratios in lungs. **d** Masson's staining showing lung section images of whole lung lobes and zoomed in areas evaluating the degree of pulmonary fibrosis at weeks 8–10 and 12–14 or saline-treated counterparts. Scale bar = 600 µm (upper panel), 200 µm (middle panels), and 50 µm (lower panels). Bar graph compares fibrotic area percentages in sections (*n* = 5 biological replicates). **e** Western blot showing FN and Col1 levels in lungs. Uncropped blots are in source data. The bar graph compares relative protein levels in mouse lungs (*n* = 4 biological replicates). **f** Hydroxyproline (HYP) content in mouse lungs. The bar graph compares HYP content in lungs (*n* = 4 biological replicates). **g** Schematic showing TAM-induced fibroblast-specific *Notch3* depletion. TAM was applied at fibrosis progression stage (week 8–9 after CS treatment). **h** Flow plots showing $NK1.1^+$(ILC1) and $ST\text{-}2^+$(ILC2) percentages in CS-treated mouse lungs (*n* = 5 biological replicates). Bar graphs compare ILC2 and ILC1 percentages in ILCs and ILC1/ILC2 ratios in lungs. **i** Schematic showing BLM-induced pulmonary fibrosis and TAM-induced fibroblast-specific *Notch3* depletion. TAM was applied at the inflammatory stage (week 1–2 after BLM treatment). **j** Flow plots showing $NKp46^+$ (ILC1) and $ST\text{-}2^+$ (ILC2) percentages in BLM-treated mouse lungs (*n* = 5 biological replicates). Bar graphs compare ILC2 and ILC1 percentages in pulmonary ILCs and ILC1/ILC2 ratios in lungs. Bar graphs represent the combined results of four biologically independent experiments with similar results. Individual values are plotted in graphs. Littermate mice were used in experiments. Data are shown as the mean ± SEM. *P* values were calculated using one-way ANOVA followed by Tukey's tests (**c**, **d**, **e**, **f**) or two-tailed unpaired Student's *t*-tests (**a**, **h**, **j**). *P* values are indicated in graphs. Source data are provided in a source data file.

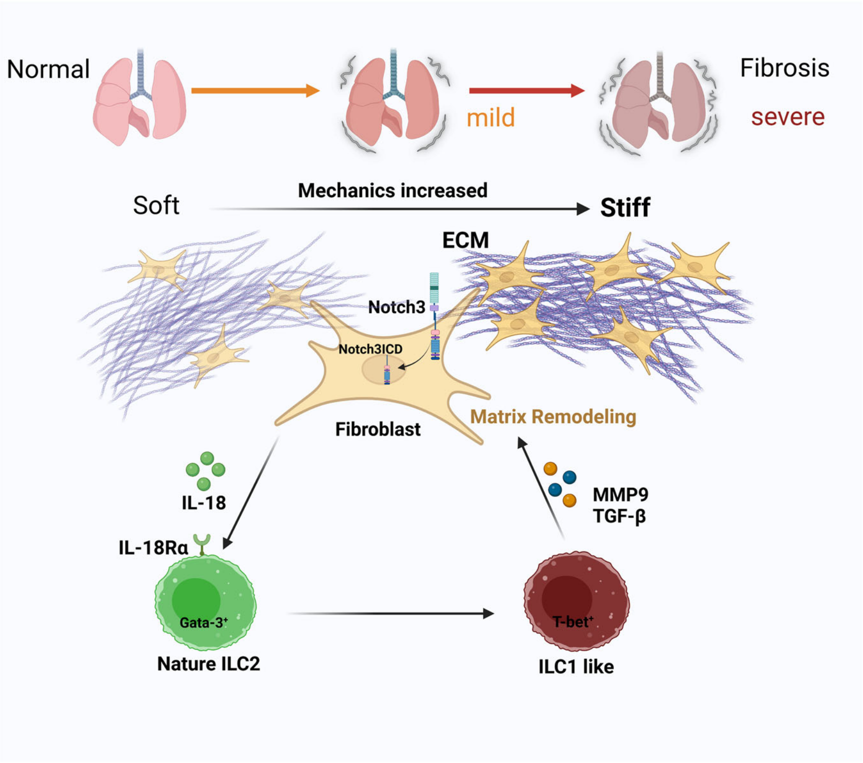

Fig. 7 | Schematic illustration that activated fibroblasts modulate ILCs plasticity in silicosis progression. Mechanics-activated fibroblasts secreting IL-18through Notch3 signaling promoted ILC2 conversion to ILC1 related to silicosis progression. Figure was partially created in BioRender. Fan, Y. (2023) BioRender.com/h98u449.

converted ILC1s in vivo, other research has highlighted their unexpected roles in tissue remodeling, in addition to IFN-γ production in mucosal inflammation. ILC1s may secrete TGF-β1 and MMP9 which modulate balanced matrix deposition and degradation[24]. A recent RNA-Seq dataset confirmed increased TGF-β1 and MMP9 expression levels in ILC1s from myocardial infarction patients[38]. Adipose ILC1s also promoted fibrogenesis by activating TGF-β1 signaling and increasing macrophage levels in an IFN-γ-dependent fashion[25]. Critically, this evidence also provided insights on ILC1 functions in silicosis. Following previous research, we verified that activated fibroblasts modulated ILC conversion and upregulated *Mmp9* and *Tgfb1* transcripts in vitro. However, converted ILC1 actions in vivo still required exploration. Notably, ILCs are composed of three distinct subsets, and their roles in silicotic fibrosis remain indistinct, but in silicosis progression, the composition of different ILC subsets changes. Herein, we reported that ILC2s converted to ILC1s, while pulmonary ILC3s also showed increasing trends. In future research, it will be worth examining if ILC2s also convert to ILC3s, as some reports have indicated that ILC2s indeed convert ILC3s in some disease pathologies[39]. If so, the identification of underlying molecular mechanisms and any associations with fibroblasts would be interesting.

ILC functions are affected by the local cytokine milieu, of which the IL-1 family is tightly linked to ILC2 conversion to ILC1. IL-18 together with IL-12 was reported to control ILC2–ILC1 conversion in COPD[17], whereas in our mousesilicosis model, no upregulated IL-12Rβ, but substantial IL-18Rα levels in ILC2s were detected, which limited the possibility that IL-12 modulated the conversion. Furthermore, by using mice with IL-18 receptor blockage, mice knocked out *Il18*, and *Rag1*$^{-/-}$*Il18*$^{-/-}$ dKO mice transferred with ILC2s, we verified a pivotal role for IL-18 in ILC conversion during silicosis progression. We also verified that ILC1/ILC2 ratios were associated with the degree of pulmonary fibrosis; a higher ratio was linked to more severe disease. Beamer and colleagues reported that *Rag1*$^{-/-}$ silicosis mice manifested more severe fibrotic phenotypes than their C57BL/6J counterparts[21], as confirmed in our study. Coincidently, we observed that ILC1/ILC2 ratios in *Rag1*$^{-/-}$ silicosis mice were significantly higher than those in wild-type silicosis mice. The more severe fibrosis and robust inflammatory responses in *Rag1*$^{-/-}$ mice were claimed be related to increased IL-18 and IL-1β expression[21], which may account for higher ILC1/ILC2 ratios. This evidence provided potential links of ILC1/ILC2 ratio to fibrosis phenotype as well as the inflammatory mediator of IL-18.

Pyroptotic macrophages are the primary cell source of IL-18, whose biological form is mediated by activated caspase 1[40]. However, in our study, we refuted that macrophages or even hematopoietic cell-derived IL-18 mediated ILC conversion in silicosis. Of note, the IL-18 cell source extended beyond leukocytes, as stromal cells emerged as another source, potentially mediating disease pathogenesis[23,41]. As key effector stromal cells in fibrogenesis, fibroblasts get activated in response to injury, where they proliferate, migrate, and promote ECM deposition[42]. Fibroblasts were previously postulated as immune-neutral cells, whose primary function was to construct and remodel the ECM. It is now garnering significant attention that fibroblasts also play immunomodulatory roles in chronic inflammatory disorders[5]. Analogous to macrophages, fibroblasts can initiate pro-inflammatory signaling pathways to facilitate leukocyte recruitment and regulate their activity[43]. NLR family pyrin domain containing 3 (NLRP3) inflammasome activation in fibroblasts may also trigger IL-18 and other pro-inflammatory cytokine release linked to tissue damage[44]. Moreover, platelet-derived growth factor receptor alpha (PDGFRα$^+$) fibroblasts in lungs were shown to express IL-33 and thymic stromal lymphopoietin (TSLP), supporting ILC2 accumulation and activation in microenvironment niches[45]. Thus, fibroblasts could sustain ILC2 viability in lungs. Similarly, we also verified a spatial correlation between fibroblasts and ILC2 in silicotic lungs and provided further evidence that activated fibroblasts modulated ILC conversion by IL-18. Analogous to our observations, lung fibroblasts, but not macrophages, may upregulate IL-18 to control CD8$^+$ T cell functions in COPD[46], suggesting the immune-modulatory potential of fibroblasts in pulmonary disorders. Even so, the immunoregulatory role of fibroblasts in chronic inflammatory diseases, particularly fibrotic silicosis, requires more study. Additionally, and of note, previous studies reported that cytokines from different cell sources in tissue microenvironments had different regulatory roles in chronic inflammatory diseases[47]. To identify multiple IL-18 cell sources, research using cell-specific *Il18* KO mice may provide new insights into IL-18 actions at different cell sources in silicosis pathogenesis.

Macrophages are believed to be critical for promoting silicosis progression, thus, depleting macrophages in lungs should theoretically alleviate fibrotic phenotypes. However, in our study, depleting AMs and IMs from lung did not significantly alleviate CS-induced pulmonary fibrosis. Moreover, ILC1/ILC2 ratios were not significantly affected in macrophage-deleted fibrotic lungs. Similar fibrotic degrees and ILC1/ILC2 ratios indicated a link between fibrogenesis and ILC conversion. These results not only demonstrated that macrophages were not key cells regulating ILC conversion during fibrogenesis, but that once fibrosis was established, it could progress under mechanical influences, but less dependent on macrophages. Mechanical hallmarks of fibrotic microenvironments are represented by both fibrosis progression outcomes and causes[48]. A stiff matrix is functionally implicated in promoting fibroblast activation, potentially generating feedback loops that propagate ECM deposition and fibrotic tissue remodeling[49]. Possibly, increased mechanics in fibrotic lungs could directly activate fibroblasts and promote fibrosis progression without relying on macrophages. However, most previous silicosis studies overlooked significant changes in the biomechanical microenvironment in fibrotic lungs and the impact on cell function. An earlier study from our group demonstrated that mechanics directly activated fibroblasts via CD44-RhoA-YAP signaling and promoted silicosis progression[50]. Blocking this pathway both ameliorated silicosis and significantly affected the lung immune microenvironment, highlighting that mechanics affected leukocyte functions. However, in this current study, we showed that a high stiff matrix did not directly convert ILC2s to ILC1s in vitro, while some studies indicated that high mechanics affected macrophage functions in fibrotic pathologies[51]. Whether mechano-transduction directly affected ILCs or other leukocyte functions in CS-induced pulmonary fibrosis remains to be explored.

In our study, we selected Notch3 as a promising molecular target which appeared to mediate mechanics-activated fibroblasts and modulate ILC conversion. Notch receptors are activators of the NLRP3 inflammasome[52], leading to chronic tissue damage and fibroblast differentiation. Notch signaling can be activated upon protease hydrolysis site exposure, triggered by pulling forces in binding ligands[53]. Of note, extrinsic pull may directly activate Notch receptors[54], thereby providing insights into how the ECM activates Notch3 in fibroblasts. Pathological stretch can also transmit pathological mechanical cues to fibroblasts and upregulate Notch3 receptor expression to form a positive feedback loop[55]. Previous studies identified interactions between Notch1 signaling and cytokine production in fibroblasts[56], while crosstalk between Notch1 and Notch3 may also exist, as observed during kidney and pancreatic damage[57,58]. Particularly, Notch3 signaling in fibroblasts has only recently emerged as a mediator regulating BLM-induced pulmonary fibrosis and RA pathology[36,37]. Also, Notch3 was the sole upregulated Notch receptor in fibroblasts from human fibrotic lungs[31]. Notch3 was reportedly involved in fibroblast activation; however, its deficiency did not directly affect fibroblast proliferation, rather, it regulated fibroblast survival and affected fibroblast viability[36]. Herein, we extend the concept that Notch3 may modulate fibroblast pyroptosis and promote pro-inflammatory cytokine (IL-18) secretion to modulate ILC conversion.

In the complex lung microenvironment, Notch3 appears to have multifunctional roles. However, previous Notch3 research was based on whole-body gene KO mice[36,37]. Brandt and colleagues advanced the field using a chimeric mouse model and suggested that in kidney fibrosis pathogenesis, cell-specific Notch3 signaling independently orchestrated leukocyte infiltration and organ fibrosis, where expression in immune cells was required for cell transmigration into tissues, while receptors expressed by kidney resident stromal cells orchestrated organ fibrosis[59]. Using cell-specific *Notch3* KO mice, we advanced the previous understanding of Notch3 signaling in silicosis pathogenesis. Notch3 signaling in myeloid cells was required for interstitial macrophage recruitment to lungs during silicosis progression[60]. Notch3 signaling in fibroblasts not only controlled pathological fibroblast expansion, but also exerted immune-modulatory effects on ILCs. This evidence provides a molecular basis suggesting that Notch3 signaling or downstream gene interference may provide additional therapeutic approaches for inflammatory and fibrotic diseases.

Our findings highlight how fibroblasts integrate into local microenvironments to regulate tissue-resident ILCs, and show that targeting the tissue-specific Notch3 signature could provide a further strategy for treating chronic inflammatory and fibrotic diseases.

Methods

Ethics statement

Our research complies with all relevant ethical regulations. The animal care and experiment protocols were approved by the IACUC (CMU2020349) of China Medical University, and complied with the National Institutes of Health Guide for the Care and Use of Laboratory Animals.

Mice

C57BL/6JGpt (Strain No. N000013), B6-*Rag1*-KO (Strain No. T004753), Il1rl1-eGFP (Strain No. T055284), *Il18*-KO (Strain No. T052436), Notch3-flox (Strain No. T007271), and CD45.1 congenic mice (Strain No. T054816) were purchased from GemPharmatech (Nanjing, China). Col1a2 Cre-ERT mice (Strain No. 029567) were purchased from the Jackson laboratory. Both male and female mice were used. Age- and sex- matched mice were used for all experiments. Littermate mice were used when possible. Mice were on a C57BL/6J background and were age and sex matched. Littermate mice were used when possible. *Rag1*$^{-/-}$*Il18*$^{-/-}$ dKO mice were crossed with *Rag1*$^{-/-}$ *and Il18*$^{-/-}$ mice. Fibroblast-specific *Notch3* KO mice were crossed with Notch3-flox and Col1a2 Cre-ERT mice. Mice were genotyped using genomic DNA (from ears) by polymerase chain reaction (PCR) using specific primers. The mice were housed in a specific pathogen-free (SPF) facility in individually ventilated cages with a temperature range of 20–26 °C and humidity levels between 40 and 70%, under a 12-h day-night cycle with ad libitum access to food and water. Mice were euthanized by carbon dioxide followed by cervical dislocation.

Crystalline silica particles

CS particles were purchased from U.S. Silica Company (Frederick, MD, USA). CS characteristics were previously described[61]. Briefly, CS particle size distribution was 97% <5 µm in diameter and 80% <3 µm in diameter, with a median diameter of 1.4 µm. Particles were washed and autoclaved for 1 h, dried, and then suspended in sterile saline. The suspension was sonicated for 10 min before use.

Mouse silicosis models and other treatments

Mouse silicosis models were established according to our previous methods[61]. Briefly, mice (7–9 weeks old) were treated with a CS suspension containing 3.0 mg particles in 50 µL saline via intratracheal administration after intraperitoneal anesthetization with pentobarbital sodium (30 mg/kg, Sigma-Aldrich). Control mice were administered the same sterile saline volume. Typical pathological silicosis processes were characterized by an acute inflammatory phase (1–2 weeks) followed by fibrotic (8–10 weeks) and severe fibrotic phases (12–14 weeks)[62]. The bleomycin (BLM)-induced lung fibrosis model was constructed by the non-invasive endotracheal intubation of BLM (Hanhui Pharmaceuticals). To induce progressive and persistent pulmonary fibrosis, mice were treated twice with BLM (1 U/kg body weight/time, total 2 U/kg body weight) with an intervention at 1 week[63]. The same sterile saline volume was applied to controls. To induce a *Notch3* KO in fibroblasts, tamoxifen (TAM) (MedChemExpress) was dissolved in corn oil (MedChemExpress) and intraperitoneally (*i.p*) injected at indicated times at a daily dose of 0.1 g/kg body weight for 7 days. Bromodeoxyuridine (BrdU) (Cat: B23151, Thermo Fisher) was used to detect ILC proliferation. A solution (1 mg in 100 µL sterile saline) was *i.p* injected into mice at 24 h before sampling.

ST2-eGFP reporter mice

A target construct expressing the eGFP-PolyA element was inserted into the translation start codon of the *Il1rl1* gene (Il1rl1-202 ENSMUST00000097772.10), and some coding exon 2 bases were deleted to generate the shift mutation. Foreign eGFP expression is dependent on the regulation of endogenous Il1rl1. *Il1rl1* was modified by CRISPR/Cas9 technology. The following process was used: a donor vector and gRNA was constructed in vitro, after which Cas9, the donor, and gRNA were microinjected into C57BL/6JGpt fertilized eggs to generate positive F0 generation mice. These mice were mated with C57BL/6JGpt mice, with pups genotyped by PCR and followed by sequence analysis. Briefly, in mice, the *Il1rl1* genome coding sequence was replaced with the eGFP coding sequence, allowing for ST2-expressing cell identification using the eGFP reporter. Mice were generated by GemPharmatech (Nanjing, China).

Single-cell isolation from lung tissues

Lymphocyte isolation from lungs was performed as previously described[7,60]. Briefly, mouse lung tissues were cut into a slurry and enzymatically digested in a solution containing type I collagenase (2 mg/mL) supplemented with DNA enzyme I (100 U/mL) in Dulbecco's Modified Eagle Medium (DMEM plus 4% bovine serum albumin (BSA)) on a rocker at 37 °C for 60 min. The cell suspension was then filtered through a 70 µm cell strainer and treated with red blood cell (RBC) lysis buffer to remove RBCs. Mononucleocytes were then enriched in a Percoll gradient solution (80%/40%) (Cytiva). Finally, a single-cell suspension was prepared for flow cytometry. LN cells were prepared by pressing tissues through a cell strainer using a sterile plunger from a 5 mL syringe.

Antibodies for flow cytometry analysis

All the antibodies used in the flow cytometry analysis were against mouse antigens. The following antibodies were purchased from BD Biosciences: mAbs specific for ST2 (U29-93), streptavidin-BV605 (Cat: 563260), and IFN-γ (XMG1.2). The following antibodies were purchased from Thermo Fisher Scientific: mAbs specific for CD25 (PC61.5), CD103 (2E7), IL-13 (eBio13A), Gata-3 (TWAJ), T-bet (4B10), BrdU (BU20A), and CD3 (17A2). The following antibodies were purchased from BioLegend: mAbs specific for CD45 (30-F11), CD3 (17A2), CD90.2 (30-H12, 53-2.1), CD127 (A7R34), ST2 (DIH9), IL-18Rα (A17071D), I-A/I-E (M5/114.15.2), ICOS (C398.4A), CD69 (H1.2F3), CXCR6 (SA051D1), Neuropilin-1 (3E12), streptavidin-PE-Cy7 (Cat: 405206), KLRG1 (2F1/KLRG1), PD-1 (29F.1A12), PD-L1 (10F.9G2), CD73 (TY/11.8), IL-17RB (9B10), CCR9 (CW-1.2), TIGIT (1G9), LAG3 (C9B7W), CD39 (Duha59), NKp46 (29A1.4), IL-18Rα (A17071D), NK-1.1 (PK136), CD45.1 (A20), CD45.2 (104), CD11b (M1/70), CD11c (N418), F4/80 (BM8), Ki-67 (16A8), CD140a (APA5), and Notch3 (HMN3-133). mAbs specific for IL-12Rβ2 (REA200) and lineage marker labeling cocktail (130-092-613) were purchased from Miltenyi. The lineage cocktail contains mAbs: CD5 (53-7.3), CD45R (B220) (RA3-6B2), CD11b (M1/70), Ly-6B.2 (REA115), Gr-1 (RB6-8C5), and Ter-119 (Ter-119).

Cell staining and flow cytometry

Flow cytometry was performed according to guidelines[64]. Dead cells were excluded from analysis using Aqua, a live/dead cell viability dye (Cat: L34957, Thermo Fisher). For surface antigen staining, cells were incubated with fluorescently labeled antibodies in staining buffer (3% fetal calf serum (FCS) in phosphate buffered saline (PBS)) at 4 °C for 30 min. After this, cells were incubated with streptavidin-BV605 secondary antibodies in PBS at 4 °C for 20 min. For transcription factor staining, cells were first stained for cell-surface markers, then fixed in 4% paraformaldehyde, permeabilized using a FOXP3/transcription factor staining buffer kit (Thermo Fisher), and stained with antibodies against transcription factors. For intracellular cytokine staining, cells were stimulated with a leukocyte stimulation cocktail containing PMA, ionomycin, brefeldin A, and monensin (Thermo Fisher) for 3–4 h before surface staining, fixation, permeabilization, and finally intracellular staining. Antibodies against transcription factors or cytokines were applied and incubated at 4 °C overnight. Flow cytometry data were acquired using BD FACS Celesta instrumentation (BD Biosciences). FACS data were analyzed using Flowjo 10.6 software (BD Biosciences). Cell counts were from the corresponding gating with collections of up to one million cell events per mice of flow analysis.

Intravascular immune cell labeling

To discriminate tissue-resident from circulating cells, we conducted a well-established intravenous (*i.v*) staining protocol, as previously described[62]. Mice were *i.v* injected with 1.5 µg of CD45-APC-Cy7 antibody (30-F11, Biolegend) diluted in 150 µL of sterile saline at 4 min before sampling.

Hematoxylin and eosin (H&E) and Masson's trichrome staining

When indicated, one lobe/lung was collected for histology and stored in 4% paraformaldehyde buffered in PBS. Lungs were embedded in paraffin and cut into 4 μm sections for H&E and Masson's trichrome staining, which was performed according to manufacturer's protocols (Solarbio). Histology images were acquired on an Aperio ScanScope and selected with ImageScope. Fibrosis-positive area quantification was performed in Image J software.

Western blotting

Cells and lung tissues were homogenized in a tissue grinder plus RIPA buffer (Beyotime). Protein levels were measured using bicinchoninic acid assays (Beyotime). Protein samples (30 μg) were separated on 8%–12% tris-glycine gels and electroblotted onto Immobilon-P Transfer Membranes (Merck Millipore). Membranes were blocked for 1.5 h at room temperature in 5% milk, and then probed with 1:500–1:1000 diluted antibodies (in 1% BSA in Tris-buffered saline plus 0.1% Tween 20). Antibodies included anti-fibronectin (EPR23110-46, ab268020, 1:1000), anti-collagen type I (Cat: 14695-1-AP, Proteintech, 1:1000), anti-Notch3 (D11B8, Cat: 5276T, Cell Signaling Technology, 1:1000). anti-β-Actin (13E5, Cat:4970S, Cell Signaling Technology, 1:5000) was used as a loading control. After three washes (10 min each), membranes were probed using secondary antibodies (Cat: 31460, Thermo Fisher, 1:2000 in 5% milk in PBS plus 0.1% Tween-20 for 1 h) linked to horseradish peroxidase. Membrane-bound proteins were detected on the ChemiDoc Touch Imaging System (BIO-RAD) using enhanced chemiluminescent western blotting detection reagents (Absin). Protein band intensities were quantified using ImageJ 1.44p software. Uncropped and unprocessed scans are supplied in the Source Data file.

ILC2 sorting

Pulmonary ILC2s were enriched by magnetic-activated cell sorting (MACS) and then examined by FACS. Mice were treated intranasally with 0.5 μg rIL-33 (Novoprotein) three times every to expand ILC2s. For MACS, an EasySep Mouse ILC2 enrichment kit was used (Stemcell Technologies, Cat: 19842) according to manufacturer's instructions. Briefly, single-cell lung suspensions were stained with lineage antibodies in MACS buffer and then incubated with anti-biotin microbeads. EasySep Magnet (Stemcell Technologies) was used to deplete lineage-positive cells. For ILC2 enrichment, the depletion was repeated twice. ILC2 populations were purified to >95%. For FACS, ILC2s were sorted using a $CD45^+lineage^-CD3^-CD90.2^+ST2^+$ alive lymphocyte strategy using BD FACSAria III instrumentation.

Adoptive transfer of ILC2s

Donor mice (CD45.1/2) were intranasally challenged with 0.5 μg rIL-33 (Novoprotein) three times every other day to expand ILC2s, which were then sorted from single-cell lung tissue suspensions (purity >98%) by FACS. Then, 5×10^5 ILC2s were intravenously transferred into *Rag1*$^{-/-}$ mice (CD45.2/2) or *Rag1*$^{-/-}$*Il18*$^{-/-}$ mice (CD45.2/2) in week 4 after CS treatment. All recipient mice were humanely sacrificed at week 12 after CS treatment.

IL-18Rα blocking antibody treatment

To block IL-18Rα signaling in vivo, mice received 10 μg of anti-IL-18Rα *i.v* injections (Catalog no. MAB12161; R&D) diluted in 150 μL sterile PBS[65], starting at week 8 every other day after CS treatment. Control mice received isotype-matched antibodies at the same dose. For analyses, mice were humanely sacrificed at 12 weeks after CS treatment.

Clodronate liposome (CL) treatment

CL (Cat: 40337ES, Yeasen Biotechnology, China) were used to deplete macrophages in vivo[66]. For circulating macrophage depletion, mice were *i.p* injected with 200 μL CL for the first time at week 7 after CS treatment. Later, mice were treated *i.p* with a dose of 100 μL CL every other day to week 12. For alveolar macrophage (AM) depletion, mice were treated *i.t.* with 10 μL of CL for one time at week 7 plus one day after CS treatment. Control mice received the same treatment but with equal PBS volumes. Mice were humanely euthanized at week 12 after CS treatment.

Bone marrow (BM) chimeras

Chimeric mice were generated using previously described methods[67]. Briefly, donor femurs and tibias were aseptically removed, and BM cells flushed out using sterile cold PBS supplemented with 2 mM EDTA. Whole BM cells were collected from C57BL/6J or *Il18*$^{-/-}$ mice. Recipients were 6–8 week old C57BL/6J mice who were irradiated with 5.5 Gy γ-radiation. Then, chimeras were established by intravenously transferring 5×10^6 BM cells into irradiated recipient mice. One week later, a silicosis model was established in BM chimeras. Mice were maintained on autoclaved water plus antibiotics (trimethoprim, Cat: T9070, sulfamethoxazole, Cat: S9641, Solarbio) and humanely sacrificed at 4–5 weeks after CS treatment.

Primary fibroblast isolation

Lung tissue was harvested, minced into 1 mm^3 pieces, and cultured in DMEM (VivaCell) plus 20% FCS (VivaCell), 100 U/ml penicillin/streptomycin (Sigma-Aldrich), 1 mM sodium pyruvate (Sigma-Aldrich), and 1× non-essential amino acids (Sigma-Aldrich). To generate fibroblasts, a "crawl-out" approach was used to culture adherent lung stromal cells[68]. Confluent cells were passaged after harvesting with trypsin-EDTA. Adherent cells were selected by repeated subculturing. Confluent cells at passages 4–6 were used in studies.

Two-dimensional (2D) cell culture and fibroblast treatments

Cells were 2D cultured using a previously described method[50]. Briefly, primary mouse lung fibroblasts or MLg2908 cells (ATCC) were grown overnight in serum deprived DMEM or EMEM (without FCS) and seeded onto coverslips or plastic dishes coated with either 1 Kappa (soft) or 25 Kappa (stiff) polyacrylamide hydrogels plus sterile collagen, following manufacturer's instructions. The 2D Col-Tgel system was purchased from Bioruo (Cat: P1720, China). After 24 h or 48 h, cells and cultured medium (CM) were collected for analyses. Primary lung fibroblasts were cultured in DMEM plus 20% FCS, 100 μ/mL penicillin/streptomycin, 1 mM sodium pyruvate, and 1× non-essential amino acids. MLg2908 cells were cultured in EMEM (VivaCell) plus 10% FCS.

Lung ILC2 culturing and treatments

ILC2s were cultured in Roswell Park Memorial Institute 1640 medium (RPMI 1640, VivaCell) supplemented with 10% FCS, 100 U/mL penicillin/streptomycin, 1 mM sodium pyruvate, and 1× non-essential amino acids, plus 10 ng/mL IL-2 (Novoprotein) and 10 ng/mL IL-7 (Novoprotein). For conditional media studies, sorted pulmonary ILC2s were cultured with conditioned media from primary lung fibroblasts stimulated by 2D Col-Tgel supplemented with fresh RPMI. After 36 h, lung ILC2s were collected for flow cytometry.

The ILC2 and fibroblast co-culturing system

ILC2s were sorted from C57BL/6J mouse lungs treated with rIL-33 (described above). Pulmonary fibroblasts were sorted from B6 or *Il18*$^{-/-}$ mouse lungs (described above). For co-culturing studies, a transwell culture system (0.4 μm aperture) (Labselect) was used. Primary lung fibroblasts (1.0×10^5 cells) were seeded in the 2D Col-Tgel system in bottom wells. After 24 h, sorted lung ILC2s (3.0×10^6 cells) were added to upper chambers in the transwell system. After co-culturing for 36 h or 60 h, lung ILC2s and fibroblasts were collected for analysis. Fibroblast and ILC2 positions were also inverted in transwell assays.

Caspase 1 activity assays

Caspase 1 activity in fibroblasts was examined using the FLICA660 caspase 1 assay kit (ImmunoChemistry Technologies, Cat: 9122). A FLICA 660 probe was used to detect cells expressing active caspase 1. Assays were performed by flow cytometry in a FLICA 660 working solution (1:60) according to manufacturer's instructions.

Bulk RNA sequencing and gene expression analysis

Using Trizol, three RNA biological replicate samples were extracted from primary lung fibroblasts (5×10^5 cells) cultured on soft (~1 kPa) and stiff (~25 kPa) matrix gels. Total RNA was qualified and quantified using an Agilent 2100 Bioanalyzer (Agilent, CA, USA). A library was prepared using the optimal dual-mode mRNA library prep kit (BGI-Shenzhen, China). cDNA library construction and sequencing were performed by BGI Global Services (BGI-Shenzhen, China) on the BGISeq platform. Raw sequencing data were then processed using SOAPnuke (v.1.5.6) to filter out low-quality reads, after which clean reads were aligned to the reference genome (*Mus musculus*, GCF_000001635.27_GRCm39, NCBI) using Bowtie2 (v.2.2.5) and HISAT2 (v.2.0.4). Based on aligned reads, gene expression levels were quantified in RSEM (v.1.2.8). Then, differential expression analysis was performed using DEseq2 (v.1.4.5) and gene expression differences between groups highlighted in volcano plots. To interpret phenotypic changes, gene ontology (GO) (http://www.geneontology.org/) and Kyoto Encyclopedia of Genes and Genomes (KEGG) (https://www.kegg.jp/) enrichment analyses were performed using Phyper based on hypergeometric tests. Significant pathway levels pathways were corrected using a rigorous threshold Q value ≤ 0.05. Gene data analyses, mining, and graphing were performed on the Dr. Tom Multi-omics Data Mining System (https://biosys.bgi.com). The volcano graph is drawn with GraphPad Prism v9. Also, a protein–protein-interaction network, with high confidence (0.900), was established using STRING based on database resources.

Immunofluorescence (IF) staining

For fibroblast IF staining, cells were washed in PBS, fixed in 4% paraformaldehyde for 15 min at room temperature, rewashed, and blocked in 5% BSA for 30 min. Cells were permeabilized in 0.5% Triton X-100 in PBS for 15 min, then stained overnight at 4 °C with anti-αSMA (Cat: 14395-1-AP, 1:100, Proteintech), Notch3 (A-6, Cat: sc-515825, 1:50, Santa Cruz Biotechnology), and IL-18 (Cat: 10663-1-AP, 1:70, Proteintech) antibodies, all diluted in PBS plus 1% FCS. After washing, cells were incubated with a fluorochrome-conjugated secondary antibody; fluorescein isothiocyanate-conjugated Affinipure Goat Anti-Rabbit IgG(H+L) (Cat: SA00003-2, 1:100, Proteintech) for 2 h, and mounted using ProLong Gold Antifade Mountant plus 4',6-diamidino-2-phenylindole (DAPI) for nuclear staining (Cat: P36941, Thermo Fisher).

IF staining of lung sections: paraffin-embedded lung sections (5 μm) were deparaffinized, after which heat-mediated antigen retrieval was performed using citrate antigen retrieval solution (Beyotime). Sections were blocked in 5% BSA in PBS for 1 h and treated with 0.25% Triton X-100 for 15 min, then stained with primary antibodies: anti-lineage (Cat: 130-092-613, 1:80, Miltenyi); anti-αSMA (Cat: 14395-1-AP, 1:100, Proteintech); and anti-Gata3-e660 (TWAJ, Cat: 50-9966-42, 1:20, Thermo Fisher), all diluted in PBS plus 1% FCS and incubated overnight at 4 °C. After washing, sections were incubated with a fluorochrome-conjugated secondary antibody recognizing α-SMA (CraLite 594-Phalloidin, Cat: PF00003, 1:200, Proteintech) for 2 h, rewashed, incubated with another fluorochrome-conjugated secondary antibody (AF488 streptavidin, Cat: 405235, 1:400, Biolegend) conjugated to biotin (Lineage) for 1 h, and mounted using ProLong Gold Antifade Mountant plus DAPI. Images were acquired using an Olympus confocal microscope.

Enzyme-linked immunosorbent assay (ELISA)

CM was collected and frozen at −80 °C. IL-18 levels in CM were assessed using an ELISA kit (Cat: DY7625, R&D) according to manufacturer's instructions. Absorbance was measured at 450 nm and 570 nm on a 96-well multimode plate reader.

Quantitative PCR (q-PCR)

Total RNA was extracted from cells in Trizol (Life Technologies) according to manufacturer's instructions and reverse transcribed to cDNA using the PrimeScript RT kit (Vazyme). Equivalent cDNA sample amounts were processed using a SYBR Green Master Mix Kit (Vazyme). The following primers were used;

Mmp9-F: CTGGACAGCCAGACACTAAAG;
Mmp9-R: CTCGCGGCAAGTCTTCAGAG;
Tgfb1-F: CTCCCGTGGCTTCTAGTGC;
Tgfb1-R: GCCTTAGTTTGGACAGGATCTG;
Gapdh-F: CATCACTGCCACCCAGAAGACTG;
Gapdh-R: ATGCCAGTGAGCTTCCCGTTCAG.

Mmp9 and Tgfb mRNA levels were determined using the $2^{-\Delta\Delta CT}$ method.

Pulmonary function measurements

Tidal volume (TV) and breathing frequency (f) values relative to body weight were used to describe pulmonary function in mice before sacrifice. DSI Buxco FinePointe NAM Non-Invasive Airway Mechanics and Buxco FinePointe Non-Invasive Airway Mechanics (NAM) (DSI, Wilmington, NC, USA) were used to record measurements.

Collagen measurements

Lungs were isolated immediately after mice were sacrificed. The collagen volume was normalized to the corresponding wet lung weight. Samples were prepared using a hydroxyproline assay kit (Nanjing Jiancheng Bioengineering Institute) and OH-proline stands tested using a UNIC 2800UV/VIS spectrophotometer according to manufacturer's instructions.

Statistical analysis

Data were presented as the mean ± SEM. Two-tailed Student's t tests for unpaired data were used for comparisons between two groups. For multigroup comparisons, one-way analysis of variance (ANOVA) with Tukey's tests were used to assess statistical significance. Statistical and linear regression analyses were performed in GraphPad Prism Software (v.9.0, GraphPad Software Inc.). All n and P values and statistical tests are indicated in figure legends. Experimental data were collected and processed randomly, and animals were randomly assigned to different experimental groups. No statistical methods were used to predetermine sample sizes, which were chosen based on previous studies. P values < 0.05 were considered statistically significant.

Reporting summary

Further information on research design is available in the Nature Portfolio Reporting Summary linked to this article.

Data availability

All data generated or analyzed during this study are provided in the manuscript, Supplementary information file and Source data file. Bulk RNA-Seq data from cultured fibroblasts are deposited in the Genome Sequence Archive database (Accession code; CRA013691). Any other details supporting the findings of the present study are available from the corresponding author upon request. Source data are provided with this paper.

References

1. Cavalin, C. et al. Beyond silicosis, is the world failing on silica hazards? *Lancet Respir. Med.* **7**, 649–650 (2019).

2. Hoy, R. F. & Chambers, D. C. Silica-related diseases in the modern world. *Allergy* **75**, 2805–2817 (2020).
3. Si, S. et al. The Australian work exposures study: prevalence of occupational exposure to respirable crystalline silica. *Ann. Occup. Hyg.* **60**, 631–637 (2016).
4. Sharma, N., Kundu, D., Dhaked, S. & Das, A. Silicosis and silicotuberculosis in India. *Bull. World Health Organ* **94**, 777–778 (2016).
5. Davidson, S. et al. Fibroblasts as immune regulators in infection, inflammation and cancer. *Nat. Rev. Immunol.* **21**, 704–717 (2021).
6. Wei, K., Nguyen, H. N. & Brenner, M. B. Fibroblast pathology in inflammatory diseases. *J. Clin. Invest.* **131**, e149538 (2021).
7. You, Y., Yuan, H., Min, H., Li, C. & Chen, J. Fibroblast-derived CXCL14 aggravates crystalline silica-induced pulmonary fibrosis by mediating polarization and recruitment of interstitial macrophages. *J. Hazard Mater.* **460**, 132489 (2023).
8. Lo Re, S., Lison, D. & Huaux, F. CD4+ T lymphocytes in lung fibrosis: diverse subsets, diverse functions. *J. Leukoc. Biol.* **93**, 499–510 (2013).
9. Puttur, F., Gregory, L. G. & Lloyd, C. M. Airway macrophages as the guardians of tissue repair in the lung. *Immunol. Cell Biol.* **97**, 246–257 (2019).
10. Vivier, E. et al. Innate lymphoid cells: 10 years on. *Cell* **174**, 1054–1066 (2018).
11. Klose, C. S. & Artis, D. Innate lymphoid cells as regulators of immunity, inflammation and tissue homeostasis. *Nat. Immunol.* **17**, 765–774 (2016).
12. Cherrier, D. E., Serafini, N. & Di Santo, J. P. Innate lymphoid cell development: a T cell perspective. *Immunity* **48**, 1091–1103 (2018).
13. Bal, S. M., Golebski, K. & Spits, H. Plasticity of innate lymphoid cell subsets. *Nat. Rev. Immunol.* **20**, 552–565 (2020).
14. Bernink, J. H. et al. Interleukin-12 and -23 control plasticity of CD127(+) group 1 and group 3 innate lymphoid cells in the intestinal lamina propria. *Immunity* **43**, 146–160 (2015).
15. Vonarbourg, C. et al. Regulated expression of nuclear receptor RORgammat confers distinct functional fates to NK cell receptor-expressing RORgammat(+) innate lymphocytes. *Immunity* **33**, 736–751 (2010).
16. Huang, Y. et al. IL-25-responsive, lineage-negative KLRG1(hi) cells are multipotential 'inflammatory' type 2 innate lymphoid cells. *Nat. Immunol.* **16**, 161–169 (2015).
17. Silver, J. S. et al. Inflammatory triggers associated with exacerbations of COPD orchestrate plasticity of group 2 innate lymphoid cells in the lungs. *Nat. Immunol.* **17**, 626–635 (2016).
18. Wang, Y., Quan, Y., He, J., Chen, S. & Dong, Z. SLAM-family receptors promote resolution of ILC2-mediated inflammation. *Nat. Commun.* **15**, 5056 (2024).
19. Zhang, J. et al. Neuropilin-1 mediates lung tissue-specific control of ILC2 function in type 2 immunity. *Nat. Immunol.* **23**, 237–250 (2022).
20. Maazi, H. et al. ICOS:ICOS-ligand interaction is required for type 2 innate lymphoid cell function, homeostasis, and induction of airway hyperreactivity. *Immunity* **42**, 538–551 (2015).
21. Beamer, C. A. et al. Innate immune processes are sufficient for driving silicosis in mice. *J. Leukoc. Biol.* **88**, 547–557 (2010).
22. Kolb, P. et al. The importance of interventional timing in the bleomycin model of pulmonary fibrosis. *Eur. Respir. J.* **55**, 1901105 (2020).
23. Nowarski, R. et al. Epithelial IL-18 equilibrium controls barrier function in colitis. *Cell* **163**, 1444–1456 (2015).
24. Jowett, G. M. et al. ILC1 drive intestinal epithelial and matrix remodelling. *Nat. Mater.* **20**, 250–259 (2021).
25. Wang, H. et al. Adipose group 1 innate lymphoid cells promote adipose tissue fibrosis and diabetes in obesity. *Nat. Commun.* **10**, 3254 (2019).
26. Wang, F. et al. Canonical Wnt signaling promotes HSC glycolysis and liver fibrosis through an LDH-A/HIF-1alpha transcriptional complex. *Hepatology* **79**, 606–623 (2024).
27. Wang, J. et al. Targeting PI3K/AKT signaling for treatment of idiopathic pulmonary fibrosis. *Acta Pharm. Sin. B* **12**, 18–32 (2022).
28. Hamanaka, R. B. & Mutlu, G. M. Our compliments to the authors: decay accelerating factor and the complement system in pulmonary fibrosis. *Am. J. Respir. Cell Mol. Biol.* **67**, 415–416 (2022).
29. Koduri, G. & Solomon, J. J. Identification, monitoring, and management of rheumatoid arthritis-associated interstitial lung disease. *Arthritis Rheumatol.* **75**, 2067–2077 (2023).
30. Meyerholz, D. K. Rigid respiration: fulminant pulmonary fibrosis after COVID-19. *eBioMedicine* **87**, 104428 (2023).
31. Reyfman, P. A. et al. Single-cell transcriptomic analysis of human lung provides insights into the pathobiology of pulmonary fibrosis. *Am. J. Respir. Crit. Care Med.* **199**, 1517–1536 (2019).
32. Nakamura, H. et al. Hypoxia-inducible factor-1alpha and poly [ADP ribose] polymerase 1 cooperatively regulate Notch3 expression under hypoxia via a noncanonical mechanism. *J. Biol. Chem.* **298**, 102137 (2022).
33. Chen, J. et al. Notch-1 and notch-3 mediate hypoxia-induced activation of synovial fibroblasts in rheumatoid arthritis. *Arthritis Rheumatol.* **73**, 1810–1819 (2021).
34. Shi, J. et al. Notch3 modulates cardiac fibroblast proliferation, apoptosis, and fibroblast to myofibroblast transition via negative regulation of the RhoA/ROCK/Hif1alpha axis. *Front. Physiol.* **11**, 669 (2020).
35. Varga, J. et al. AKT-dependent NOTCH3 activation drives tumor progression in a model of mesenchymal colorectal cancer. *J. Exp. Med.* **217**, e20191515 (2020).
36. Vera, L. et al. Notch3 deficiency attenuates pulmonary fibrosis and impedes lung-function decline. *Am. J. Respir. Cell Mol. Biol.* **64**, 465–476 (2021).
37. Wei, K. et al. Notch signalling drives synovial fibroblast identity and arthritis pathology. *Nature* **582**, 259–264 (2020).
38. Li, J., Wu, J., Zhang, M. & Zheng, Y. Dynamic changes of innate lymphoid cells in acute ST-segment elevation myocardial infarction and its association with clinical outcomes. *Sci. Rep.* **10**, 5099 (2020).
39. Zhang, K. et al. Cutting edge: notch signaling promotes the plasticity of group-2 innate lymphoid cells. *J. Immunol.* **198**, 1798–1803 (2017).
40. Hachim, M. Y., Khalil, B. A., Elemam, N. M. & Maghazachi, A. A. Pyroptosis: the missing puzzle among innate and adaptive immunity crosstalk. *J. Leukoc. Biol.* **108**, 323–338 (2020).
41. Jarret, A. et al. Enteric nervous system-derived IL-18 orchestrates mucosal barrier immunity. *Cell* **180**, 50–63 e12 (2020).
42. Barkauskas, C. E. & Noble, P. W. Cellular mechanisms of tissue fibrosis. 7. New insights into the cellular mechanisms of pulmonary fibrosis. *Am. J. Physiol. Cell Physiol.* **306**, C987–C996 (2014).
43. Bhattacharyya, S. et al. TLR4-dependent fibroblast activation drives persistent organ fibrosis in skin and lung. *JCI Insight* **3**, e98850 (2018).
44. Sandanger, O. et al. The NLRP3 inflammasome is up-regulated in cardiac fibroblasts and mediates myocardial ischaemia-reperfusion injury. *Cardiovasc. Res.* **99**, 164–174 (2013).
45. Dahlgren, M. W. et al. Adventitial stromal cells define group 2 innate lymphoid cell tissue niches. *Immunity* **50**, 707–722 e706 (2019).
46. Yun, J. H. et al. Hedgehog interacting protein-expressing lung fibroblasts suppress lymphocytic inflammation in mice. *JCI Insight* **6**, e14457 (2021).
47. Hung, L. Y. et al. Cellular context of IL-33 expression dictates impact on anti-helminth immunity. *Sci. Immunol.* **5**, eabc6259 (2020).
48. Long, Y., Niu, Y., Liang, K. & Du, Y. Mechanical communication in fibrosis progression. *Trends Cell Biol.* **32**, 70–90 (2022).
49. Tschumperlin, D. J., Ligresti, G., Hilscher, M. B. & Shah, V. H. Mechanosensing and fibrosis. *J. Clin. Invest.* **128**, 74–84 (2018).
50. Li, S. et al. Targeting mechanics-induced fibroblast activation through CD44-RhoA-YAP pathway ameliorates crystalline silica-induced silicosis. *Theranostics* **9**, 4993–5008 (2019).

51. Wang, Y. et al. Stiffness sensing via Piezo1 enhances macrophage efferocytosis and promotes the resolution of liver fibrosis. *Sci. Adv.* **10**, eadj3289 (2024).
52. Jin, Y. et al. Jagged1-mediated myeloid Notch1 signaling activates HSF1/Snail and controls NLRP3 inflammasome activation in liver inflammatory injury. *Cell Mol. Immunol.* **17**, 1245–1256 (2020).
53. Luca, V. C. et al. Notch-Jagged complex structure implicates a catch bond in tuning ligand sensitivity. *Science* **355**, 1320–1324 (2017).
54. Gordon, W. R. et al. Mechanical allostery: evidence for a force requirement in the proteolytic activation of notch. *Dev. Cell* **33**, 729–736 (2015).
55. Wang, J. et al. S1P induces proliferation of pulmonary artery smooth muscle cells by promoting YAP-induced Notch3 expression and activation. *J. Biol. Chem.* **296**, 100599 (2021).
56. Lee, S. et al. Contribution of autophagy-Notch1-Mediated NLRP3 inflammasome activation to chronic inflammation and fibrosis in keloid fibroblasts. *Int. J. Mol. Sci.* **21**, 8050 (2020).
57. Song, H. Y., Wang, Y., Lan, H. & Zhang, Y. X. Expression of Notch receptors and their ligands in pancreatic ductal adenocarcinoma. *Exp. Ther. Med.* **16**, 53–60 (2018).
58. Kavvadas, P. et al. Notch3 orchestrates epithelial and inflammatory responses to promote acute kidney injury. *Kidney Int.* **94**, 126–138 (2018).
59. Brandt, S. et al. Fibrosis and immune cell infiltration are separate events regulated by cell-specific receptor Notch3 expression. *J. Am. Soc. Nephrol.* **31**, 2589–2608 (2020).
60. Yuan, H. et al. Crystalline silica-induced proinflammatory interstitial macrophage recruitment through Notch3 signaling promotes the pathogenesis of silicosis. *Environ. Sci. Technol.* **57**, 14502–14514 (2023).
61. Li, C. et al. Blocking the 4-1BB pathway ameliorates crystalline silica-induced lung inflammation and fibrosis in mice. *Theranostics* **6**, 2052–2067 (2016).
62. You, Y. et al. Crystalline silica-induced recruitment and immuno-imbalance of CD4(+) tissue resident memory T cells promote silicosis progression. *Commun. Biol.* **7**, 971 (2024).
63. Redente, E. F. et al. Persistent, progressive pulmonary fibrosis and epithelial remodeling in mice. *Am. J. Respir. Cell Mol. Biol.* **64**, 669–676 (2021).
64. Cossarizza, A. et al. Guidelines for the use of flow cytometry and cell sorting in immunological studies (third edition). *Eur. J. Immunol.* **51**, 2708–3145 (2021).
65. Ghose, P. et al. The interaction between IL-18 and IL-18 receptor limits the magnitude of protective immunity and enhances pathogenic responses following infection with intracellular bacteria. *J. Immunol.* **187**, 1333–1346 (2011).
66. Moreno, S. G. Depleting macrophages in vivo with clodronate-liposomes. *Methods Mol. Biol.* **1784**, 259–262 (2018).
67. Misharin, A. V. et al. Monocyte-derived alveolar macrophages drive lung fibrosis and persist in the lung over the life span. *J. Exp. Med.* **214**, 2387–2404 (2017).
68. Edelman, B. L. & Redente, E. F. Isolation and characterization of mouse fibroblasts. *Methods Mol. Biol.* **1809**, 59–67 (2018).

Acknowledgements

Research reported in this publication was supported by the National Natural Science Foundation of China (No. 82173490 to Chao Li).

Author contributions

Y.H. and F.Y. conducted majority of experiments and performed data analysis. L.Y. contributed to the western blot analysis. H.Y., Y.Y., Y.C., X.W., and H.M. participated in a number of experiments and assisted with mice breeding and genotyping identification. C.L., Y.H., and F.Y. drafted and revised the manuscript. C.L. and Y.H. conceived the project. C.L. and J.C. supervised the study.

Competing interests

The authors declare no competing interests.

Additional information

Supplementary information The online version contains supplementary material available at https://doi.org/10.1038/s41467-024-54174-5.

Correspondence and requests for materials should be addressed to Jie Chen or Chao Li.

Peer review information *Nature Communications* thanks Kjetil Ask and the other, anonymous, reviewer(s) for their contribution to the peer review of this work. A peer review file is available.

Reprints and permissions information is available at http://www.nature.com/reprints